nature biomedical engineering

Article

https://doi.org/10.1038/s41551-025-01605-3

A filamentary soft robotic probe for multimodal in utero monitoring of fetal health

Received: 22 October 2024

Accepted: 11 December 2025

Published online: 26 January 2026

Check for updates

Hedan Bai[1,2,17] ✉, Jianlin Zhou[1,17], Mingzheng Wu[1,17], Steven Papastefan[3,4,17], Xiuyuan Li[5,6,17], Haohui Zhang[5], Kaiyu Zhao[1,7], Zhuoran Zhang[1,7], Wei Ouyang[1], Catherine R. Redden[3], Amir M. Alhajjat[3,4], Heyang Wang[1,8], Yibo Zhou[1,9], Kenneth Madsen[1,10], Shuo Li[1], Andrew I. Efimov[1,11], Katelyn Ma[1,11], Lisa Kovacs[1,8], Sahdev Patel[1,12], Daniel R. Liesman[3,4], Katherine C. Ott[3,4], Rinaldo Garziera[13], Steffen Sammet[14], Wenming Zhang[6], Yonggang Huang[1,5,7,8] ✉, Aimen F. Shaaban[3,4] ✉ & John A. Rogers[1,7,8,11,15,16] ✉

Fetal surgery offers valuable opportunities to address severe congenital disabilities, yet accurate evaluation of fetal physiological changes during in utero procedures to mitigate the risk of operative complications remains an unmet need. Conventional unimodal approaches lack predictive value, specificity and compatibility with minimally invasive interventions. Here we present a bioelectronic system featuring a multimodal, steerable filamentary probe that interfaces directly with the fetus in utero, enabling reliable and minimally invasive monitoring of various physiological parameters. Integrated soft robotic actuators ensure consistent contact through controlled navigation and force delivery, creating a gentle and secure interface with delicate fetal surfaces. In a sheep fetal surgery model, the multifunctional probe effectively monitored in utero conditions during fetoscopic surgeries, detecting fetal bradycardia, hypoxia and hypothermia, potentially informing for early intervention. Experimental results on rodents and large animal fetuses demonstrate potential for direct translation to human use. This system offers continuous, comprehensive fetal monitoring, addressing gaps in current clinical practices, and provides real-time insights during fetal surgeries.

Advances in fetal surgery create unique interventional opportunities to reduce the morbidity and mortality associated with severe congenital disabilities that affect approximately 3% of live births in the United States[1–3]. Fundamental challenges exist, however, in evaluating fetal physiological changes during in utero procedures, resulting in a high risk of operative complications and fetal death. The physical constraints in the uterus and the invasiveness of conventional procedures limit direct access to the fetus[4]. These difficult circumstances hinder the development of reliable and comprehensive monitoring modalities for continuous, real-time evaluation of changes in the vital signs of the fetus[5]. Conventional techniques, such as cardiotocography, primarily monitor heart rate as a measure of fetal health, which is often a late indicator of fetal compromise[5–7]. While intermittent fetal ultrasound provides additional information on fetal well-being, it provides only brief snapshots of fetal physiology during temporary breaks in a relatively long fetoscopic operation and may therefore miss

A full list of affiliations appears at the end of the paper. ✉e-mail: hedan.bai@mat.ethz.ch; y-huang@northwestern.edu; ashaaban@luriechildrens.org; jrogers@northwestern.edu

critical aberrations that signify developing fetal distress. Furthermore, accurate echocardiographic characterization of ductus venosus flow, valvular regurgitation, ventricular contractility and middle cerebral artery peak systolic velocity are sensitive to movement and highly dependent on the quality of the sonographic window, which is technically difficult to consistently achieve in the CO_2/amniotic fluid bubble.

Emerging skin-interfaced bioelectronic technologies, including those for fetal electrocardiography[8–10], phonocardiography[11,12], magnetocardiography[13,14] and pulse oximetry[15,16], have some potential for collecting fetal physiological data across the maternal abdominal wall[17]. Although these technologies are non-invasive, they suffer from poor specificity and strong irregularities owing to fetal–maternal signal confluence, leading to inconsistent and inaccurate fetal measurements, especially during in utero procedures that require dynamic manipulations of the uterus and fetus[18]. Furthermore, advances in fetal surgery techniques from larger, open hysterotomies to less invasive fetoscopic intervention increase the need for physically compatible platforms that are capable of immediate identification of abnormal fetal vital signs[19,20]. A miniaturized, flexible and physically controllable in utero fetal interface that supports multimodal monitoring represents the type of platform that could provide effective, real-time fetal evaluation during fetal surgeries.

Here we present a bioelectronic system with these features, enabling reliable and minimally invasive monitoring of fetal heart rate (FHR), arterial blood oxygen saturation (SpO_2), core temperature (T) and electrocardiogram (ECG) data, in the form of a multimodal, steerable filamentary probe that directly interfaces with the fetus[21–23]. Integrated soft robotic actuators ensure reliable contact with the fetus through navigation and force delivery under external control[24]. In utero fetal monitoring during fetoscopic surgeries in a sheep model demonstrates the effectiveness of this multifunctional probe. Results indicate that measurements of experimentally controlled fetal bradycardia, hypoxia and hypothermia facilitate early detection and treatment of abnormal fetal vital signs during both open and fetoscopic repair of spina bifida, one of the primary indications for fetal surgery in humans. Moreover, the filamentary designs and soft actuator-assisted deployment mechanisms create broad-ranging opportunities in fetal monitoring, including prenatal testing and labour. These capabilities in real-time, continuous and comprehensive vital monitoring of fetuses address unmet needs in fetal surgery practices, enabling clinicians to evaluate a wide range of source physiological parameters in fetoscopic surgery.

Flexible fetal probe design

The soft robotic fetal probe (SRFP) combines multimodal, miniaturized electronic sensors with small-scale soft robotic actuators, integrated together onto a flexible, filamentary probe that allows endoscopic coaxial deployment through a standard 10 French (3.4 mm inner diameter) cannula for intraoperative monitoring during fetoscopic surgery (Fig. 1a). Sensors for fetal vital signs lie along a thin (~160 μm), 1-mm-wide flexible printed circuit board (fPCB), coated with parylene as an encapsulating layer. The modalities include a reflective pulse oximeter formed with microscale, inorganic light-emitting diodes (μ-ILEDs) that emit at red and infrared wavelengths, and photodiodes (μ-IPDs) that detect backscattered light from these μ-ILEDs to reveal FHR and SpO_2 through photoplethysmogram (PPG) data, a thermistor to monitor fetal temperature, and microelectrodes (4 mm × 1 mm) to detect fetal ECG (Fig. 1b,c). The soft robotic actuators include those for bi-directional flexion, torsion and expansion, wrapped around the probe or bonded to its back surface. These actuators allow the user to control bending (up to 180°, curvature $\kappa \approx 0.2\ mm^{-1}$) to geometrically conform the sensors to various curvilinear fetal interfaces, twisting (up to 540°) to continuously adjust the orientation of the sensors to tissue surfaces and expanding (up to 6 mm diameter) to gently press the sensors into intimate contact (Fig. 1d). With appropriate control over flexion and torsion, the proximal end of the probe, carrying miniature sensors, can smoothly insert into fetal lumen and expand at a point of interest to create physical contact for reliable measurements during dynamic fetal surgery with minimal slippage at the interface (Fig. 1e). A battery-powered data transmission module connects to the fetal probe at the distal end and is placed outside of the maternal body (Supplementary Fig. 4), digitizing and processing raw physiological biosignals with an onboard microcontroller, which then transmits the data wirelessly in air to the user interface via Bluetooth Low Energy (BLE). The circuit-level integration of wireless electronic modules on the PCB (proximal hardware; Supplementary Fig. 1) allows clinicians to position the entire device close to the operative field, enabling the immediate start of data collection after the probe is deployed and secured through a standard fetoscopic port alongside the fetoscope or fetoscopic instruments.

After achieving contact with the fetus, the electronic modules perform onboard computation of real-time data to provide synchronous monitoring of fetal SpO_2, heart rate, temperature and ECG, graphically displayed on a separate user interface. This intraoperative monitoring capability allows for real-time detection of fetal hypoxia, hypothermia, bradycardia and arrhythmia, thereby alerting surgeons to any distress for immediate rescue interventions (Fig. 1f). Multimodal monitoring of this type provides essential insights into the co-evolution of features of abnormal fetal vital signs under various surgical conditions, thereby creating unique and important insights during in utero procedures.

Soft robotic actuator design and optimization for in utero probe deployment

A series of microfabrication procedures allows for miniaturization of the soft robotic actuators and simplification of the manufacturing process for the microscale channels for pneumatic and/or hydraulic control[25–27] (Extended Data Fig. 1 and Supplementary Fig. 2). This approach features a zero-initial-volume channel design combined with patterns of thin films of polyimide (that is, parallel fibres for bending and oblique fibres for twisting) that act as inextensible strain-limiting layers. A rolling process integrates these films into the probe platform before encapsulation within another layer of silicone. The result of this construction is to convert uniform expansion into anisotropic actuation, with sufficient load capacity and performance parameters that exceed those of other miniaturized soft robotic actuator designs (Supplementary Table 1).

Figure 2 (Supplementary Video 1) summarizes details associated with soft robotic flexion, torsion and expansion. Figure 2a,b highlights mechanisms for flexion at different angles, either isolated (free) from or integrated (load) with the probe. A 180° flexion angle for free and load states can be achieved with pressures of 53.2 kPa and 94.5 kPa, respectively; both values are within the range of those provided by syringe compressors commonly used in catheterization procedures. Similarly, the torsion actuators operate at pressures below 50 kPa for all angles, either integrated or isolated (Fig. 2c,d). The twisting actuator reaches an angle of 180° for free and load states with pressures of 25.6 kPa and 44.6 kPa, respectively. For the balloon actuator, the height reaches 5 mm under a pressure of 7.4 kPa, with a maximum strain of 260% at the top of the balloon (Fig. 2e,f and Extended Data Fig. 4). Numerical and experimental characterizations of sensor securement shows that the force for pulling away a probe scales approximately linearly with increased pressure after the actuator expansion reaches the inner diameter of tubes (metal and silicone, inner diameters 3.4 mm) (Supplementary Fig. 3). Experiments further validate the ability of the expansion module to anchor the probe within an 8-gauge metal tube (Supplementary Video 2) and within a compliant hydrogel lumen that replicates tissues, such as the fetal rectum and esophagus (Supplementary Video 3). The bi-directional flexion module can steer the probe in

https://doi.org/10.1038/s41551-025-01605-3

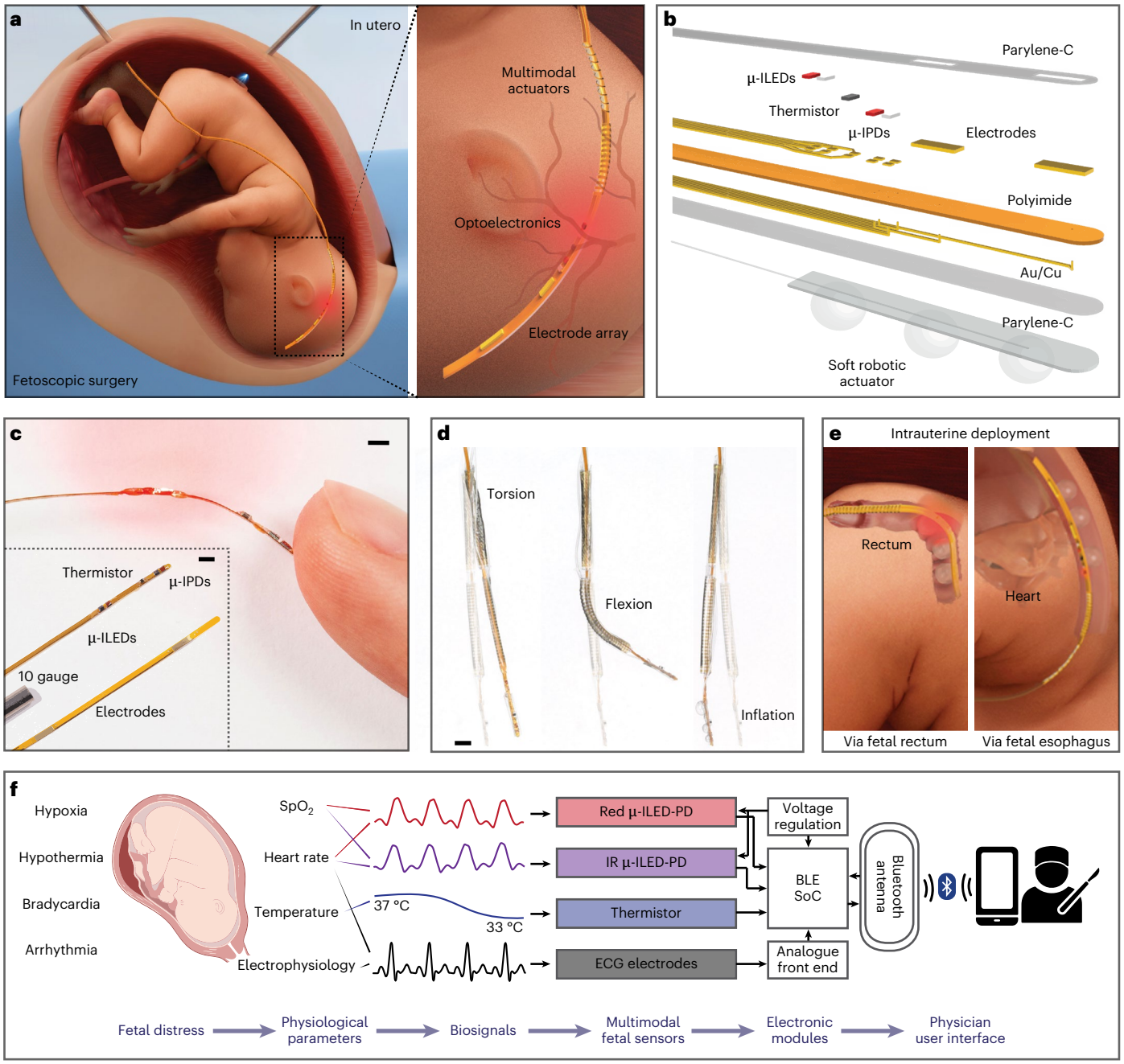


Fig. 1 | Filamentary, soft robotic probe for multimodal in utero monitoring of fetal health. a, Schematic illustration of the SRFP for minimally invasive physiological monitoring during fetal surgery. **b**, Exploded view schematic illustration of the portion of the system that establishes the fetal interface. **c**, Photograph of a device. Inset: top view of the photoplethysmography (PPG) optoelectronics and bottom view of the ECG electrodes. Scale bar, 3 mm. **d**, Torsion, flexion and balloon inflation initiated by multimodal soft robotic actuation. Light, before actuation; opaque, after actuation. Scale bar, 5 mm. **e**, Schematic illustration of SRFP intrauterine navigation through fetal rectal and esophageal approaches. **f**, Schematic block diagram of the system and the study design for fetal physiological monitoring. Schematic illustrations used materials created by BioRender.com.

a related phantom with narrow branches (Supplementary Video 4). All three modules can actuate safely without physical damage to the hydrogel (Supplementary Video 3). The maximum principal strains on the silicone layers, the copper layer on the probe and the polyimide patterns are within their elastic limits across all actuator operations[28] (Extended Data Figs. 2 and 3). The predominant failure mode occurs at the edges of the actuator chamber, where delamination between the top and bottom layers may develop under high-pressure conditions (Extended Data Fig. 2 and Supplementary Fig. 4). Extensive simulations and ex vivo experiments provide the basis for optimizing the parameters in these designs (Extended Data Figs. 4 and 5).

The soft robotic system enables probe deployment into fetal luminal structures that are readily accessible during fetal surgery, supporting various physiological sensing modalities[29]. Combining three modules, the soft robotic actuators enable the sensory probe to navigate constrained and delicate environments inside the body with good steerability (Supplementary Note 1, Supplementary Fig. 5 and Supplementary Video 3), fine torsional control (Supplementary Note 2) and device securing (Fig. 2h), while ensuring gentle device–tissue interaction (Supplementary Note 3, Supplementary Fig. 6 and Supplementary Video 4). Figure 2g shows the ultrasound-assisted deployment of a probe into the fetal esophagus, to support an interface

https://doi.org/10.1038/s41551-025-01605-3

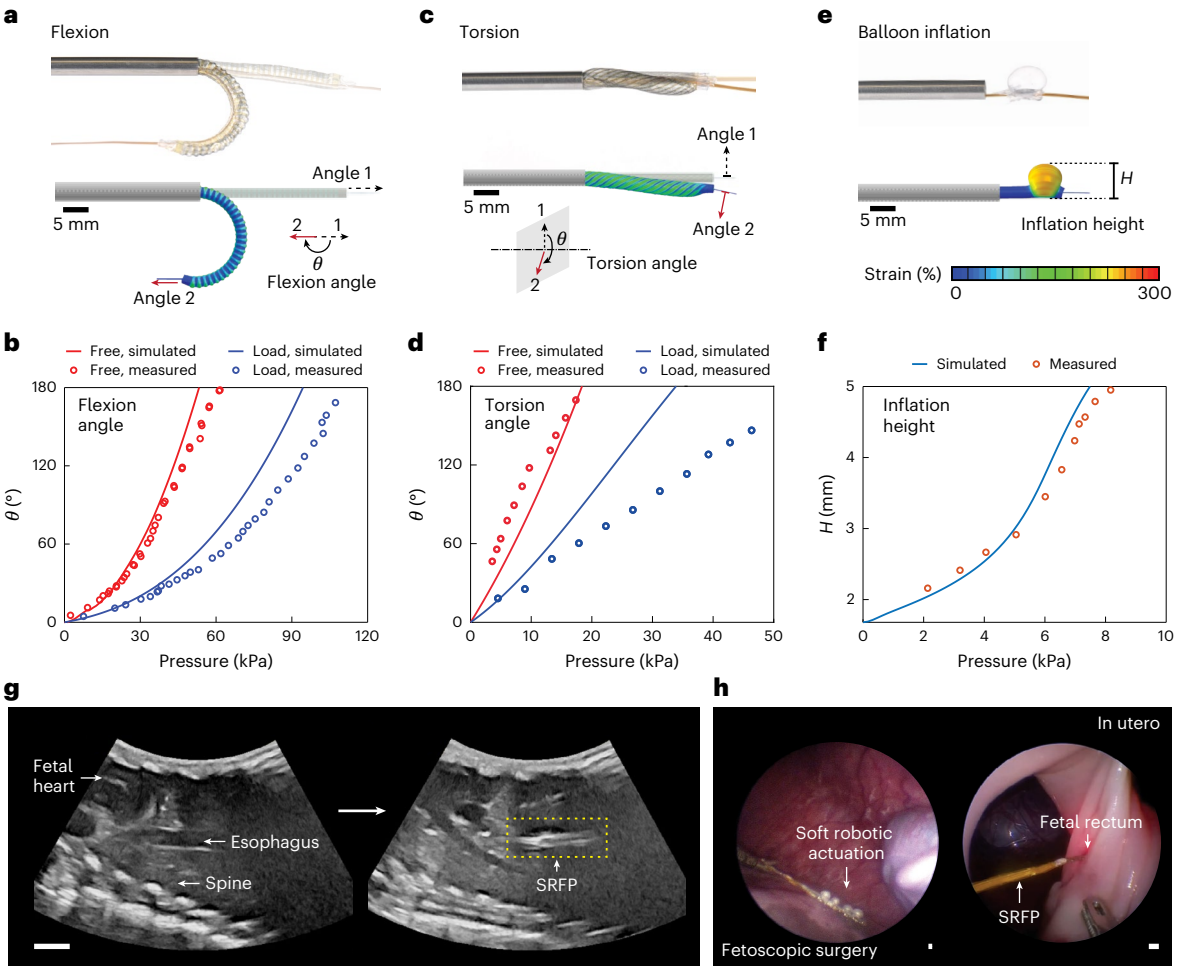


Fig. 2 | Numerical and experimental characterization of the soft robotic component of the system. a, Experimental characterization and finite element simulations for the flexion actuator. **b**, Simulated and measured flexion angle at different pressures applied to the microfluidic channel for actuation with or without mechanical loading of the probe. **c**,**d**, Same as **a** and **b**, but for the torsion actuator. **e**, Same as **a**, but for the balloon inflation actuator. **f**, Simulated and measured inflation height at different applied pressures. **g**, Ultrasound-assisted deployment of a probe into the fetal esophagus. Scale bar, 10 mm. **h**, Photograph of deployment and soft robotic actuation during fetoscopic surgery on a fetal lamb. Scale bar, 1 mm.

in proximity to the fetal heart for cardiac electrophysiology measurement. Figure 2h and Supplementary Video 5 illustrate the process of in utero deployment of a probe with expanding actuators, aimed to obtain PPG and temperature data during fetoscopic surgeries. In this fetoscopic surgery on a fetal lamb, after inserting an unactuated miniature probe into the uterus through a fetoscopic port, the surgeon guides the soft and flexible probe into the fetal rectum. From outside the uterus, injection of saline through a syringe expands the actuator ballons. After activating the wireless module, the probe collects high-fidelity data without motion artefacts associated with slippage at the tissue interface (Supplementary Fig. 7 and Supplementary Video 5).

Characterization and optimization of electrical and optical sensing modalities

Red and infrared (IR) light penetrates tissues, and the backscattered light captures heart rate and the fraction of oxyhaemoglobin (HbO_2) relative to total haemoglobin (for example, SpO_2). These optical signals track the relative change in light absorption of the pulsatile and non-pulsatile signals at 660 nm and 940 nm, where the molar extinction coefficient spectra of oxyhaemoglobin (HbO_2) and deoxyhaemoglobin (Hb) exhibit a large contrast. The probe designs optimize high perfusion index (PI = AC/DC, the ratio of pulsatile to non-pulsatile signals) to better resolve fetal physiological parameters based on optical sensing[30]. Design choices result from Monte Carlo simulations of perfusion index as a function of position of the μ-IPD for fixed placement of the μ-ILED and artery (Fig. 3a). The perfusion index increases with distance from the μ-ILED along the longitudinal direction of the artery, suggesting that a larger distance between the μ-ILED and the μ-IPD enables higher signal quality[31], which is confirmed by the experimental data in Fig. 3b with measurements from a human finger. The measured signal-to-noise ratio (SNR), however, decreases substantially at large separations (>15 mm). In addition, Monte Carlo simulation shows that penetration depth and illumination volume depend on illumination intensity in the expected way. The perfusion index remains constant, and the SNR increases with μ-ILED intensity (Supplementary Fig. 8). The probes here balance these considerations by use of a separation distance of 10 mm and adjustable μ-ILED intensity to optimize optical performance.

Measurements of fetal physiological parameters during open surgery on fetal lambs (Fig. 3c) define strategies for deploying this sensor platform for in utero PPG monitoring. Experiments during open fetal lamb surgery at 75 days of gestation (equivalent to approximately 22–23 weeks of human gestation) assess the placement of the sensing interface on various fetal structures where the distance to the underlying arteries or arterioles varies. These structures include the neck, chest, abdomen, back and limbs, as well as within intraluminal locations such as the rectum and esophagus of a fetal lamb weighing

https://doi.org/10.1038/s41551-025-01605-3

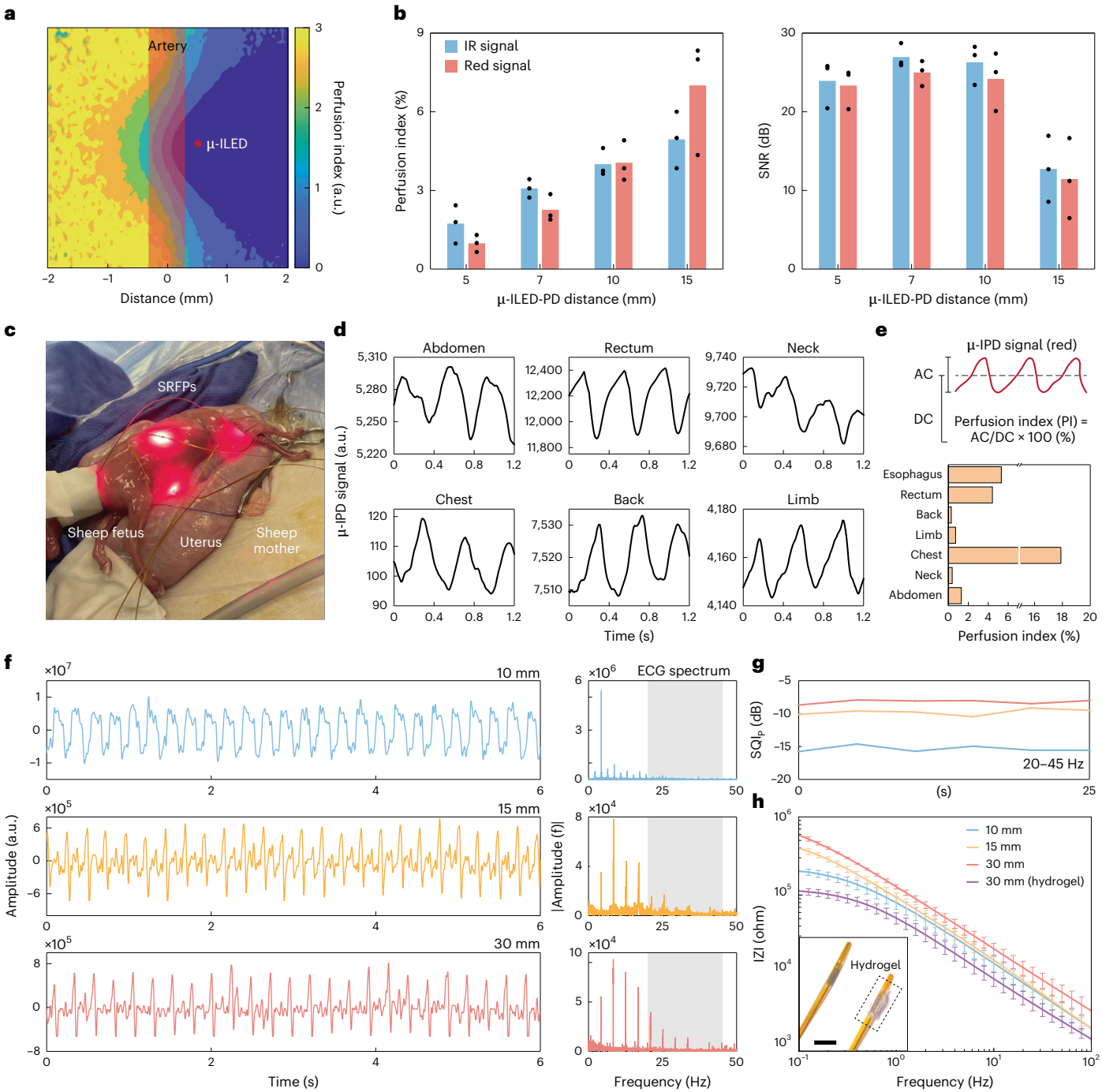


Fig. 3 | Numerical and experimental characterization of the physiological sensors. a, The perfusion index distribution. **b**, Left: perfusion indices of red and IR signals at different μ-ILED-PD separation distances on human palm and finger. Right: red and IR PPG SNR at various μ-ILED-PD separation distances. $n = 3$ subjects in each group. **c**, SRFP deployment during open fetal lamb surgery. **d**, Representative μ-IPD signals at different sensing positions of a fetal lamb during open fetal surgery. **e**, Top: calculation of perfusion index from raw μ-IPD signals. Bottom: comparison of perfusion index across deployment locations on the fetal lamb during open fetal surgery. **f**, Waveform and frequency spectrum of ECG signal recorded from an adult mouse using SRFP with different ECG electrode distances. **g**, Ratio of the power spectral densities between the overall ECG signal spectrum and the QRS complex spectrum (signal quality index, SQI_P) at different ECG electrode distances from an adult mouse model. **h**, Agar-based artificial tissue–electrode contact impedance |Z| at different ECG electrode separation distances, with and without solid hydrogel (scale bar, 5 mm). Data are presented as mean values ± s.d. $n = 3$ independent devices in each group.

approximately 0.5 kg. While the sensors capture pulsatile behaviour at all locations (Fig. 3d), the perfusion indices vary widely. Specifically, the chest wall location yields the maximum perfusion index (17.9%). This result is consistent with that from experiments on an adult mouse model, where the chest yields PPG signal with the highest perfusion index as it is a central location closer to the heart (Supplementary Note 4 and Supplementary Fig. 9). Acceptable values are achieved from placement into more translationally relevant locations such as the fetal rectum and esophagus (4–6%). Insufficient values result from the back, limb, neck and abdomen (0.3–1.6%) (Fig. 3e). Given that robust stability is more readily attainable with probe placement into fetal luminal structures that are remote from the surgical site, the rectum and esophagus represent preferred locations for monitoring during fetal surgery.

https://doi.org/10.1038/s41551-025-01605-3

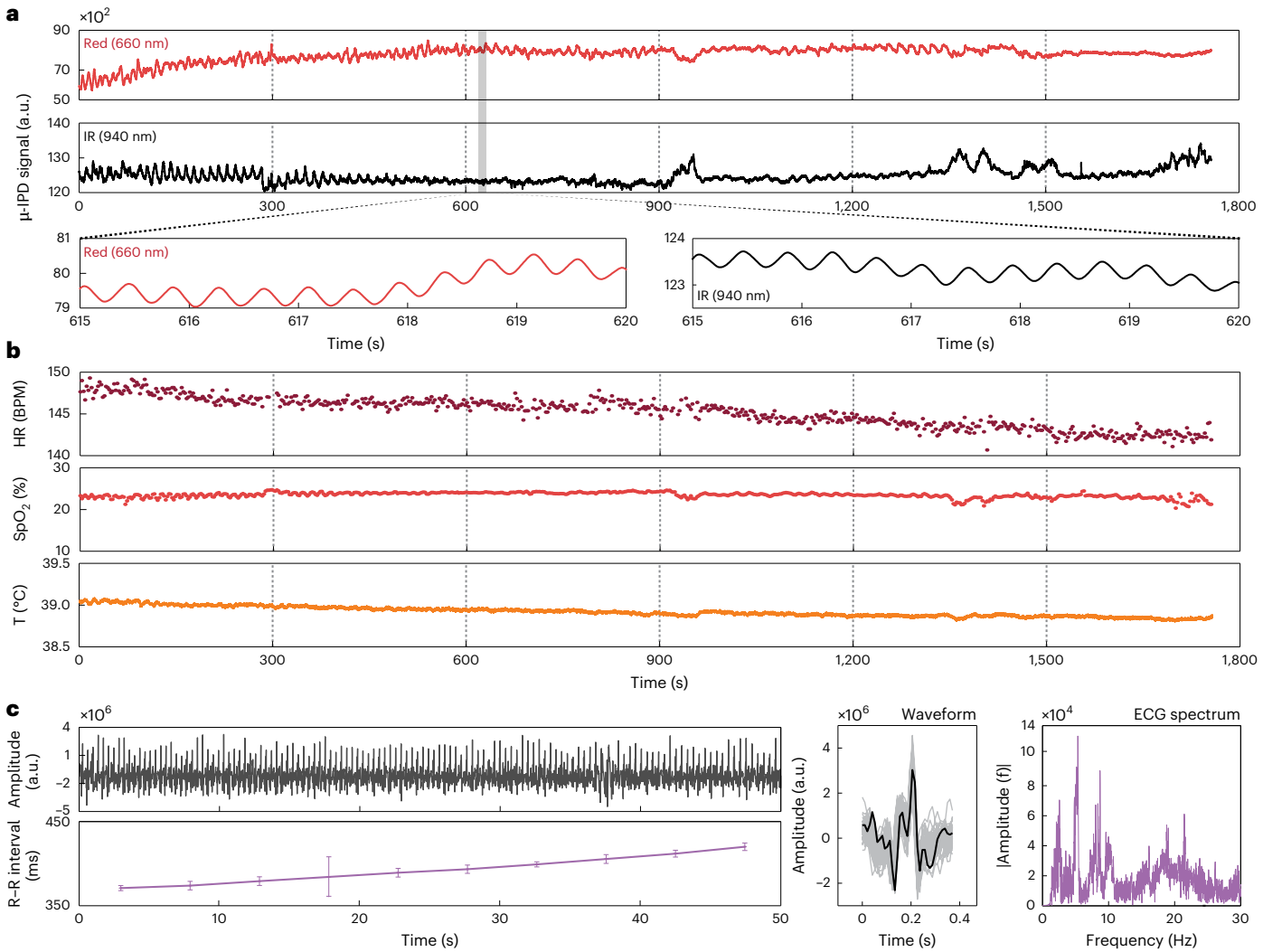


Fig. 4 | In utero real-time fetal physiological sensing during fetoscopic lamb surgery. a, μ-IPD signals recorded during continuous in utero fetal monitoring in fetoscopic surgery. **b**, Physiological parameters, including heart rate, SpO_2 and core temperature, computed from the sensed biosignals. **c**, Representative intra-esophageal fetal ECG recording. Left: a 50 s continuous intra-esophageal ECG recording with the extracted average R–R interval every 5 s. Data are presented as mean values ± s.d. Middle: averaged traces showing the ECG waveform recorded from SRFP. Grey: individual ECG waveform traces. Right: frequency spectrum of the recorded ECG data shows the frequency characteristics.

The separation distances and the sensing positions strongly influence the morphology and quality of the ECG signals[32]. In vivo experiments on adult mouse models guide selection of choices in the separation distance to optimize for distinctive features of the QRS complex[33,34]. The ratio between the power spectral densities of the overall ECG signal spectrum (0–50 Hz) and the QRS complex spectrum (20–45 Hz) defines the ECG signal quality index ($SQI_p = 10\log_{10}(\frac{\int_{20}^{45} P(f)df}{\int_{0}^{50} P(f)df})$, dB)[35,36]. This parameter increases as the separation distance extends from 10 mm to 30 mm (Fig. 3f). Studies with rodents reveal that deployments in the intra-esophagus location offer much stronger ECG signals than those in the rectum (Extended Data Fig. 6). Additional experiments confirm this conclusion and also demonstrate the responsiveness of the ECG recordings to physiological changes and their alignment with PPG data (Extended Data Figs. 7 and 8).

Electrical impedance spectroscopy indicates expected impedance (ohm) and phase (θ) values for the Au electrodes over a relevant frequency range (1 Hz to 10^5 Hz), with insensitivity to bending across various angles (Supplementary Fig. 10). A conductive solid hydrogel cast around the electrode pads[37,38] reduces the impedance by approximately 60% (Fig. 3g), to facilitate collection of high-quality ECG waveforms at large separation distances[39,40].

Multimodal real-time fetal monitoring during sheep fetoscopic surgery

A series of fetal physiological recordings during in utero (Supplementary Video 5) and ex utero procedures confirm the feasibility of multimodal, real-time monitoring with this platform. As fetal bradycardia is a late measure of fetal compromise, assurance of fetal well-being requires comprehensive, real-time monitoring of multiple physiological parameters. Figure 4a shows representative red and IR PPG signals throughout a 30 min fetoscopic spina bifida procedure on a fetal lamb, demonstrating stable, high-quality signal collection despite substantial fetal manipulation during the repair[41]. Real-time (Fig. 4b; for details, see Methods) analysis yields values of FHR, which in this case are stable with only minimal fluctuation. The fetal SpO_2, experimentally calibrated with intermittently sampled arterial blood gas values (Extended Data Fig. 9), also remains stable at around 23% throughout the surgery. The fetal core temperature remains at 39 °C. Collectively, the physiological parameters revealed by multimodal fetal sensing are within normal ranges, confirming an absence of

https://doi.org/10.1038/s41551-025-01605-3

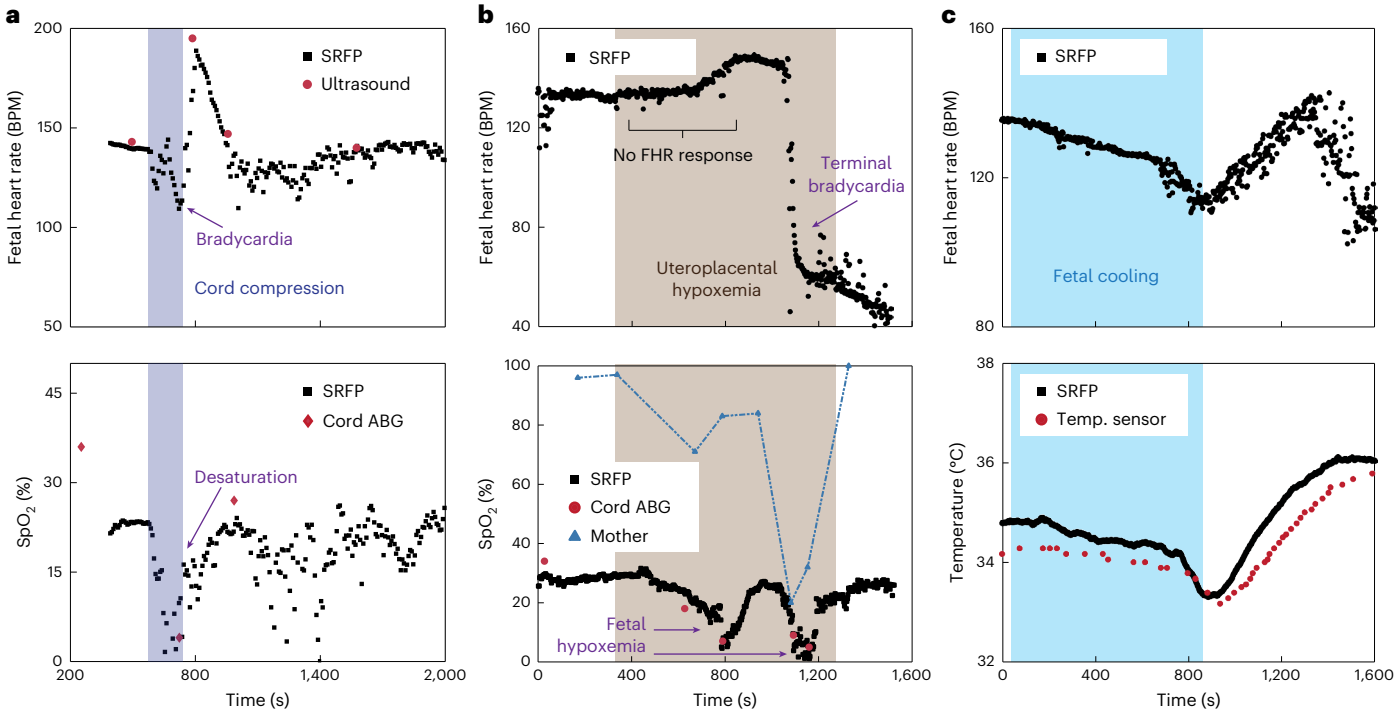


Fig. 5 | Multimodal continuous fetal lamb monitoring during open fetal surgery reveals fetal physiologic derangement in experimentally controlled scenarios. a, Top: fetal probe recording of FHR response to cord compression with intermittent ultrasound validation. Bottom: fetal probe recording of fetal SpO_2 response to cord compression with intermittent cord ABG validation. **b**, Top: same as **a**, but for uteroplacental hypoxemia. Bottom: same as **a**, but for uteroplacental hypoxemia with intermittent sampling of SpO_2 from the mother. **c**, Top: fetal probe recording of FHR response to hypothermia. Bottom: fetal probe recording of fetal core temperature with intermittent validation from a temperature sensor.

fetal physiologic derangement during fetoscopic repair, beyond the capability of fetal echocardiography alone.

Longitudinal recordings of fetal ECG are also possible with probe placement within the esophagus (Fig. 4c), to yield complete electrophysiological waveforms, along with FHR and heart rate variability based on R–R intervals[42,43]. This endo-esophageal interfacing strategy is also utilized in complex open fetal surgery such as ex utero intrapartum treatment, enabling reliable monitoring of fetal physiological parameters during such sophisticated procedures[44–47] (Extended Data Fig. 10).

In vivo validation and monitoring of fetal physiological derangement

Physiological monitoring during episodes of experimentally controlled fetal or maternal hypoxia in open surgery on fetal lambs serves to validate the feasibility of real-time detection of fetal physiologic derangement with SRFP. Figure 5a illustrates the multimodal fetal response to umbilical cord compression. Upon constriction of the umbilical cord, the fetus exhibits bradycardia and hypoxia, which both resolve spontaneously after the release of temporary cord compression. Throughout this process, intermittent fetal echocardiography, a common practice used as a gold-standard FHR measurement in this study, reveals the same trend in changes in heart rate. Compared with sonographic evaluation, the SRFP offers the same accuracy in heart rate monitoring while providing continuous heart rate tracking with much higher temporal resolution. This continuous real-time tracking reveals events such as instantaneous bradycardia that would otherwise be missed with intermittent ultrasound measurements. In addition, arterial blood gas (ABG) analysis from the umbilical cord before, during and after cord compression indicates similar trends in hypoxia[48,49].

Subsequent evaluations determine the fetal physiological response to experimentally induced maternal hypoxia, whereby reduction in the oxygen supply leads to maternal oxygen desaturation (Fig. 5b). Maternal hypoxia eventually leads to a reduction of fetal SpO_2, continuously monitored by the probe and intermittently validated with fetal cord ABG, with two distinct hypoxic events observed. In one event, minimal changes in FHR accompany mild fetal hypoxia, while in the other, terminal bradycardia during severe hypoxia leads to fetal demise. These episodes demonstrate the necessity for multimodal fetal monitoring. Unimodal monitoring of FHR alone can miss episodes of mild to moderate fetal hypoxia that are potentially treatable before the development of terminal bradycardia, as substantial heart rate changes may only represent late manifestations of severe fetal hypoxia conditions.

Additional studies involve experimentally induced fetal hypothermia that may occur owing to fetal exposure during fetal surgery. Figure 5c shows that fetal core temperature in the rectum slowly decreases during fetal cooling and gradually recovers following fetal warming. A commercial thermometer inserted into the fetal esophagus validates the measurements with the probe. During this process, the fetal probe captures a similar gradual decrease in FHR as the fetal core temperature decreases, followed by an increase in FHR during rewarming. However, the changes in FHR do not reach traditional thresholds for bradycardia (FHR < 110) and the fetal cooling events are likely missed with fetal echocardiography alone until critical fetal hypothermia develops.

Additional clinical significance of SRFP in fetal surgery

The ability to capture high-quality fetal physiological monitoring data with the SRFP extends its clinical applications. Specifically, morphology analysis of fetal pulse waveforms and real-time warnings of abrupt changes in fetal vital signs represent two potential directions for this technology. Pulse wave analysis extracts characteristic features of pressure waveforms to infer functional properties of the cardiovascular

https://doi.org/10.1038/s41551-025-01605-3

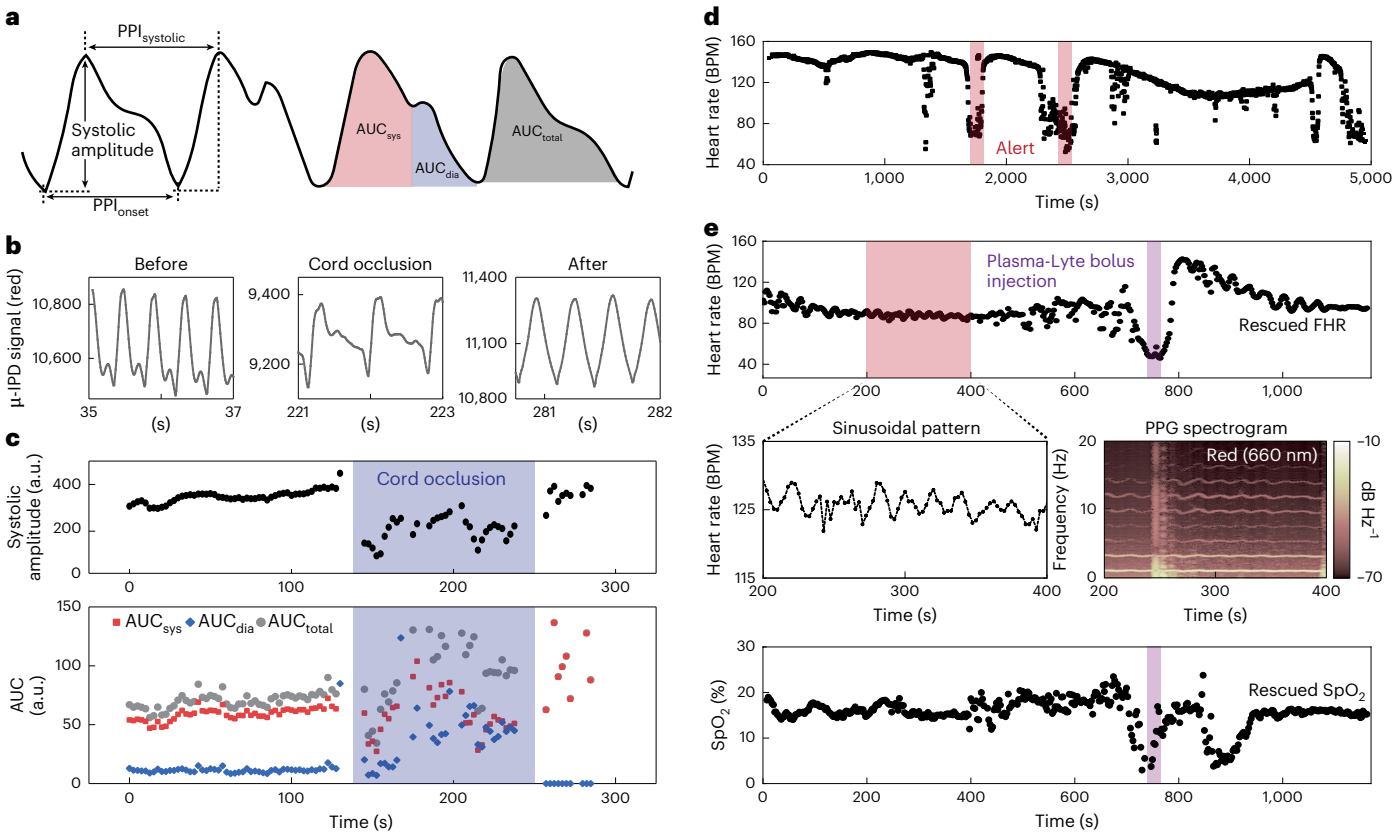


Fig. 6 | Pulse wave analysis and emergency intervention for critical fetal physiologic derangement of fetal lambs during open fetal surgery. a, Features of PPG waveform. $PPI_{systolic}$, interval between the systolic peaks of adjacent pulses. Systolic amplitude, amplitude of systolic peak signal from baseline; AUC_{sys}, systolic area under the curve; AUC_{dia}, diastolic area under the curve; AUC_{total}, total pulse area under the curve. **b**, PPG waveform morphologies before, during and after cord occlusion. **c**, Top: systolic amplitude before, during and after cord occlusion. Bottom: AUC_{sys}, AUC_{dia} and AUC_{total} before, during and after cord occlusion. **d**, Alert and recovery of spontaneous fetal cardiac decompensation (that is, fetal decelerations followed by bradycardia) during induced maternal hypothermia. **e**, Early detection of abnormal fetal vital signs from an unexpected sinusoidal pattern and intervention before the onset of spontaneous fetal bradycardia. Top: FHR before and after Plasma-Lyte bolus injection. Middle left: unexpected sinusoidal FHR pattern before the onset of spontaneous fetal bradycardia. Middle right: PPG spectrogram from the red μ-IPD signal.

system based on arterial haemodynamics[14,17,50] (Fig. 6a). Pulsatile signals collected from the transrectal monitoring of the fetal lamb during open fetal surgery exhibit distinct waveform morphologies influenced by the onset of umbilical cord occlusion (Fig. 6b). A pulse wave analysis algorithm (Supplementary Fig. 11; details in Methods) extracts from the raw data the systolic amplitude and the pulse area under the curve (AUC)[50]. Figure 6c shows that during cord occlusion, the systolic amplitude decreases sharply, indicating a decreased blood volume passing through the umbilical cord to the fetus[51]. Changes in AUC indicate that the mean arterial pressure first decreases and then quickly increases during occlusion. The increasing contribution of diastolic AUC is consistent with an increase in pulse wave reflection in this process. After cord compression, the complete loss of diastolic AUC reflects loss of the dicrotic notch following the systolic waveform, a finding that may reflect reflexive changes in vascular tone after cord compression in the fetus[52]. Derivative features of the pulse waves can also be extracted (Supplementary Figs. 11 and 12), showing characteristic peaks and valleys where the ratios provide insights into other physiological parameters such as vascular stiffness[53,54]. Although pulse wave analysis approaches that rely on mechanisms of arterial haemodynamics in adults are well established, little is known for fetuses. The technology introduced here may serve as a powerful tool for the characterization of fetal pulse waveforms that may improve the understanding of fetal haemodynamics during surgical interventions.

Continuous multiparameter monitoring is fundamentally important in open and fetoscopic surgery, as it enables the early detection of abnormal fetal vital signs, facilitating timely rescue interventions that help ensure the safe completion of the procedure. Figure 6d illustrates a representative episode of spontaneous fetal cardiac decompensation, where fetal deceleration developed into critical fetal bradycardia during open fetal spina bifida repair and is identified by the SRFP, triggering the administration of rescue fetal stimulation and cardiac compressions. Figure 6e shows another case where the SRFP detected the development of spontaneous sinusoidal heart rate patterns during open fetal surgery that indicate potential acute fetal anaemia, which subsequently led to fetal bradycardia[55]. The FHR recovers with crystalloid resuscitation, allowing for the continuation of surgery. Notably, while the fetal SpO_2 decreases at the time of Plasma-Lyte bolus injection (Fig. 6e, bottom, ~750 s) resulting from a potential blood dilution artefact, the SRFP also detects fetal hypoxia when the FHR exhibits severe sinusoidal patterns (Fig. 6e, bottom, ~850 s). This observation aligns with the association between fetal hypoxia and sinusoidal heart rate patterns[56]. Examination of safety during in vivo operation relied on histological analysis of the fetal rectum following probe use during a fetoscopic procedure. The results show no preliminary evidence of mechanical or thermal damage to the fetal rectal mucosa (Supplementary Fig. 13). Altogether, these findings demonstrate the ability of the SRFP to continuously monitor multiple fetal physiological parameters simultaneously, with the potential to expand clinical understanding of various fetal physiological derangements during open fetal or fetoscopic surgery.

Discussion

This work introduces a multimodal soft robotic probe as a minimally invasive platform for monitoring essential parameters of fetal health. This platform offers continuous and comprehensive monitoring of fetal vital signs, addressing an unmet need in fetal surgical practices. The operating capabilities meet the requirements of fetal surgeries by providing real-time continuous measurements of FHR, blood oxygenation, temperature and ECG simultaneously. The miniature form factor and flexible mechanical attributes facilitate minimally invasive use in both fetoscopic and open fetal surgeries, with robust monitoring quality largely unaffected by surgical procedures. The deployment of the probe into the uterus only requires standard instruments that are readily accessible during fetal surgery. In addition to advanced sensing modalities, the combination of miniaturized soft robotic actuators with flexible, filamentary optoelectronic systems creates a gentle and secure interface to delicate, irregular and curvilinear fetal surfaces. Furthermore, the wireless mode of communication with external monitors minimizes the potential for interference with the array of sophisticated surgical equipment required for these surgical procedures.

A range of experiments presented here demonstrate the clinical utility of the probe in various applications, including continuous monitoring of the early vital sign changes that may indicate fetal compromise, detection of different types of fetal derangement, presentation of real-time intraoperative warnings for rescue interventions and expansion of the knowledge of fetal physiology through the study of multimodal fetal signals. These experimental and validation results in the sheep model indicate the potential of this platform for direct translation to human fetuses for open and fetoscopic surgery, particularly as the fetal sheep model is the established large animal platform for fetal surgical practice before transitioning to human[57,58].

Considerations related to the safety of the probe were evaluated in benchtop and in vivo studies. The SRFP uses common materials approved for implantable medical devices (Supplementary Note 5). The short-term use as an intraoperative monitor (typically 2–6 h) avoids the potential for any long-term adverse reactions. The primary potential safety concerns are thus related to mechanical and thermal effects. Evaluations of the latter indicate minimal increases in temperature local to the probe. Benchtop experiments of soft robotic actuation yield information on the former. For each actuation module, the operating pressures are lower than the burst pressures (Supplementary Note 3), and the safety factors remain valid during simultaneous use of multiple actuations, as each operates independently without additive effects on pressure.

As shown in a benchtop simulation of a human fetus within the uterus (Supplementary Video 6), the multimodal soft robotic actuators enable single-port (8-gauge) deployment by activating different actuation modes to steer, adjust and conform the sensors onto various fetal locations (for example, rectum, leg, chest and ankle) selected for good signal quality. Further engineering advances may allow the probe to be deployed with 16-gauge needles used for amniocentesis with wireless capabilities for prenatal monitoring during pregnancy[59,60]. Future work may also allow for integration of sensors of additional parameters, such as fetal pH and CO_2, thereby enabling continuous monitoring of an expanded range of fetal biomarkers of interest.

Methods

Fabrication of the soft robotic actuators

The fabrication process began with spin coating (1,000 rpm for 45 s) and curing the first silicone layer (Ecoflex 00-31, Near Clear) on a 4-inch acrylic disc substrate in a heating oven at 75 °C for 30 min. A 50-µm-thick polyimide mask film was cut with an ultraviolet laser (Protolaser U4, LPKF) and laminated onto the partially cured Ecoflex surface[61]. Screen printing with anti-bonding spray (Ease Release 200) and permanent ink (METAL PRO, ZEYAR) was used to mark and create zero-thickness fluidic channels. After removing the channel mask, the second silicon layer (Ecoflex 00-31, Near Clear) was spin-coated (1,500 rpm for 45 s) and cured in the heating oven at 75 °C for 5 min. Laser-cut polyimide (10 µm thick) reinforcement patterns were then placed over the marked channels. The third outer silicone layer (Dragon Skin 30, Smooth-On) was spin-coated (1,000 rpm for 45 s) on top of the patterns and cured in the heating oven for 8 h. Soft robotic actuator outlines were cut and peeled off from the substrate. A dip-coated thin silicone tubing was bonded with the first silicone layer using silicone resin (Ecoflex 00-31, Near Clear) and rolled onto the silicone tube to transform the 2D actuators into a 3D catheter actuator.

Assembly and encapsulation

The flexible probe PCB consists of 5 layers: a 25-µm-thick polyimide substrate, 18-µm-thick top and bottom Cu layers, and two 12-µm-thick polyimide cover layers on the top and bottom Cu layers. Hot-air soldering with a low-temperature indium solder bonded the red µ-ILED (LA HR43WP3, DComponents) and IR µ-ILED (LA MI40WP4, DComponents) pairs to their respective pads. Optical epoxy (NOA 63, Norland Products) was used to cover the µ-ILEDs, and ultraviolet light was used to cure the epoxy for 3 h. Silicon adhesive (Kwik-Sil) is applied to the junction where the epoxy meets the flexible PCB. Without a neutral mechanical property between the rigid and flexible sections, cracks may form, potentially leading to liquid damage to the µ-ILED. ECG Cu electrode pads (4 mm × 1 mm) are coated with 25 nm of gold using immersion plating. Chemical vapour deposition was then used to form conformal coatings of 30 µm parylene-C, encapsulating the device. A polyimide tape mask was used to cover the electrode pads before coating, and the pads were exposed after the tape was removed.

Circuit designs

The wireless electronics circuit was designed using EAGLE 9.6 (Autodesk). A low-dropout linear voltage regulator (NCP114AMX330TCG, Onsemi) in UDFN packaging (1 mm × 1 mm) converted the battery DC voltage to a constant voltage supply (3.3 V) to power the digital integrated circuits (ICs). A BLE microcontroller (NRF52832, Nordic Semiconductor) in QFN packaging (6 mm × 6 mm) with a custom embedded programme served as the CPU and Bluetooth communication. The BLE system-on-chip (SoC) was connected to a miniaturized (3.2 mm × 1.6 mm) ceramic antenna (2450AT18A100, Johanson Technology) for data transmission. Other passive components (resistor, capacitor and inductor) are with 0201 (imperial) and 0402 packaging. Two micropower, zero-input crossover distortion amplifiers (ADA4505-1, Analog Devices) served as transimpedance amplifiers, amplifying both the PD signal and thermostat signal. A second low-dropout linear voltage regulator (NCP114AMX330TCG, Onsemi), connected to the battery, was connected to two SP3T switches (CL-SB-13B-01T, Nidec Components). These switches are connected to different resistors to select various current outputs for the red and IR µ-ILEDs. An ultra-low-power, high common-mode noise rejection (>100 dB) biopotential analogue front end (MAX30003, Maxim Integrated) in TQFN packaging (5 mm × 5 mm) amplified, filtered and digitized the ECG signals and transmitted the data to the BLE SoC via the serial peripheral interface (SPI) interface.

Mechanical modelling and simulations

The commercial software Abaqus (2023, Dassault Systems Simulia) was used to assess the mechanical characteristics of the device. The assembled device consists of three parts: the actuator, the probe and the patterns. The actuator, probe and rectum tissue phantom were modelled using tetrahedron (C3D10H) elements. The pattern was modelled using shell (S4) elements. The minimal element size was about 1/4 of the thickness of the elastomer layer. Geometrical nonlinearity was considered in the simulation, and the mesh convergence was validated. The Ogden model was used to describe the actuator material Ecoflex 00-31 (EF) and Dragon Skin 30 (DS) silicone, with hyperelastic

parameters fitted from reference data[62]: μ_{EF} = 23 kPa, α_{EF} = 2.79, D_{EF} = 0.002 kPa^{-1}, and μ_{DS} = 137 kPa, α_{DS} = 2.79, D_{DS} = 0.001 kPa^{-1}. The Young's modulus and Poisson ratio of probe and tissue phantom are given by E_{Cu} = 119 GPa and ν_{Cu} = 0.34, $E_{polyimide}$ = 2.5 GPa and $\nu_{polyimide}$ = 0.34, and E_{tissue} = 12 kPa and ν_{tissue} = 0.49 (ref. 63). The pattern was fixed in the actuator using embedded constrain. The probe was wrapped by the actuator, and contact interaction was imposed between the probe and the inner surface of the actuator. For free expansion, bending and twisting simulation, one end of the probe was fixed, and a uniform pressure was imposed on the chamber surface. The rotation angle of the other end of the probe was recorded. In the pulling force simulation, a Coulomb friction model captured the frictional interaction between the actuator and the phantom. A gradually increasing pulling force defined the maximum force just before slippage.

Experimental set-up for mechanical characterization

Characterization of expansion height, bending angle and twisting angle. One side of the actuator was fixed horizontally on a retort stand. The actuator was connected to an injector (30 ml, fill with air) on a syringe and a pressure gauge (B40, ASME) by pipes and a three-way valve. During the actuation process, the flow speed of the syringe pump was set to 5 ml min^{-1}, to achieve a quasi-static deformation. A digital camera (Z7, Nikon) was placed perpendicular to the actuator and recorded the deformation of the actuator and the pressure. The motion analysis software (Tracker, version 6.15) was used to obtain the rotation angle of the actuator. For characterization of expansion height, a ruler was placed beside the actuator at the same plane, for scaling the expansion height in the photos.

Characterization of pulling force. A puncture needle tube and a silicone rectum phantom were fixed on the tensile testing machine (Mark-10 digital force gauges). The phantom has an inner diameter of 4 mm, an outer diameter of 10 mm and a length of 45 mm. These dimensions approximate the fetal rectum at approximately 24–28 weeks of gestation, based on anatomical data. The phantom used low-modulus platinum-cure silicone (for example, Ecoflex-type, Smooth-On), as a soft, tissue-like compliance suitable for simulating fetal rectal tissue. One side of the expansion actuator was inserted into the tube, and the other side was connected to the moving stage of the tensile testing machine through a force gauge. A pressure was applied to the actuator, and then the actuator was pulled out of the tube by a speed of 0.05 mm s^{-1}. The maximum friction force during the pulling process was recorded as the pulling force at applied pressure.

Experimental set-up for electrode characterization

The impedance spectrum of the electrode was measured in 0.1 M PBS at room temperature using a digital potentiostat (Metrohm Autolab) with an Ag–AgCl reference electrode and a Pt counter electrode. The same potentiostat was used for both the bending test and the contact impedance test on the Au electrodes of the probe at room temperature and 27 °C, with 0.1 M PBS and agar-based artificial tissue (composed of 0.92 wt% agarose, 2.29 wt% sodium chloride, 0.57 wt% glycerol and 96.22 wt% deionized water). The solid hydrogel is composed of 14.95 wt% polyvinyl alcohol, 37.37 wt% glycerol, 0.15 wt% potassium disulfite, 23.23 wt% propylene glycol, 1.87 wt% potassium chloride and 22.43 wt% DI water. The mixture was initially heated to 95 °C until it became clear and was then poured into a 2 mm deep arc-shaped mould. The electrode probe was positioned on the mould, and the hydrogel was used to encapsulate and secure the probe by allowing it to pass through the holes adjacent to the electrodes. The hydrogel was then cured at −20 °C for 24 h.

Optical simulations

The Monte Carlo method is applied to simulate the light transport within tissue and artery structures[64,65]. The tissue is modelled as a semi-infinite medium, while the artery is modelled as a cylinder with a radius of 3 mm, oriented parallel to the tissue surface at a depth of 5 mm. Both the tissue and artery are voxelated, creating a simulation space of 140 × 140 × 85 voxels, each with a side length of 0.5 mm. Geometry outside this region is ignored owing to the negligible light intensity, and expanding the simulation space does not affect the results. A red μ-ILED is located at the centre of the tissue's surface, while an IR μ-ILED is located 1 mm to the right of the red μ-ILED. To ensure accuracy, 5×10^9 photons are simulated for each μ-ILED. The angular distribution of the μ-ILED light is described using a Lambertian emission profile. The red μ-ILED has a wavelength of 645 nm, while the IR μ-ILED has a wavelength of 950 nm. The tissue absorption coefficient μ_a = 0.056 mm^{-1} and the reduced scattering coefficient μ'_s = 0.55 mm^{-1} for red light, whereas for IR light μ_a = 0.046 mm^{-1} and μ'_s = 0.45 mm^{-1} (ref. 66). In the artery, μ_a = 0.17 mm^{-1} and μ'_s = 1.54 mm^{-1} for red light, while μ_a = 0.65 mm^{-1} and μ'_s = 1.25 mm^{-1} for IR light[67]. The refractive indices (n) is 1.4 for both the tissue and artery[68]. Supplementary Fig. 7 plots the intensity profiles of red and IR light when viewed along the axis of the artery. The total emission power of each μ-ILED is 1 W. The fluence contours for 0.1 W mm^{-2} and 0.01 W mm^{-2} are highlighted.

Human experiments for optical sensing characterization

Human experiments were performed by placing the probe sensor on the palm and finger, with the μ-ILED and PD separated by varying distances to characterize optical signal performance. Pulse waveforms were recorded continuously from 3 healthy volunteers (ages 20–35) for approximately 3 min per measurement. All participants provided informed consent before the experiments, and the study protocol was approved by the Institutional Review Board of Northwestern University (STU00220375).

Animal models

Animals were managed according to the protocols approved by Northwestern University and University of Chicago Animal Care and Use Committees. The study involved wild-type C57BL/6 mice, obtained from Charles River and bred internally. Both adult male and female mice, aged 80–120 days, were included. Before procedures, all mice were group housed, maintained at approximately 25 °C, 30–70% humidity, and fed a standard diet under a 12 h/12 h light/dark cycle (lights on at 6:00 or 7:00). Only healthy, immunocompetent mice that had not participated in previous procedures were used. Mice were anaesthetized with isoflurane (3% for induction, 1.5–2% for maintenance) and secured on a small animal stereotaxic frame (David Kopf Instruments) for recordings with a fetal probe. After monitoring ECG and PPG, the mice were euthanized using isoflurane.

All fetal surgeries were performed on pregnant Katahdin sheep, obtained from Purdue University, at gestational ages of 77–125 days. The ages of gestation were determined by timed mating. Determination of the presence of singleton, twin or triplet gestation occurred before arrival to the animal facility. Ultrasound enabled confirmation of the viability of the pregnancy after arrival and before any procedure. Lamb fetuses of 75 days roughly correlate to a 22–23-week human fetus, 95 days roughly to a 25–26-week human fetus with respect to neurodevelopment, and 125 days reach maturity similar to a 37–40-week (full-term) fetus[69].

In vivo sheep fetal spina bifida validation studies

On the day before surgeries, ewes were fasted and slow-release buprenorphine (0.27 mg kg^{-1}) was administered intramuscularly. For fetal spina bifida repair operations, spinal defects were created during the duration of a separate open fetal surgical operation at the gestational age of 75 days according to the previously described surgical technique[70]. In brief, sheep were positioned supine, and general endotracheal anaesthesia was induced using 0.4 mg kg^{-1} midazolam, 10 mg kg^{-1} ketamine and 6 mg kg^{-1} propofol titrated to effect and maintained with 1–3% isoflurane. Ewes were monitored continuously using

standard intraoperative monitoring devices of blood pressure (arterial line), pulse oximetry (maternal ear), temperature (nasal), end-tidal carbon dioxide and 3-lead ECG. A baseline fetal echocardiogram (ECHO) was performed before starting the procedure. Infraumbilical midline laparotomy was performed to expose the uterus, and a 6 cm hysterotomy was created to externalize the fetus in the case of open fetal surgery. Bupivacaine dosed at 1–2 mg kg^{-1} was injected into the incision after closure for maternal pain control. All fetuses were given intramuscular 'cocktail' injections of rocuronium, atropine and fentanyl that were dosed according to the estimated fetal weight before defect creation and repair. Spinal defects were created by removing the skin and paraspinous musculature overlying the lower thoracic spine to the mid-sacrum inferiorly and the iliac crest laterally. An L1–L5 laminectomy and durectomy was created sharply. A posterior sagittal longitudinal myelotomy was performed in the exposed spina cord. The fetus was then returned to the amniotic cavity, amniotic fluid replaced with lactated Ringer's and the hysterotomy and laparotomy closed with layers of monofilament suture.

Spina bifida repair was performed between gestational ages of 90 and 105 days via an open hysterotomy or fetoscopic repair technique using four 3 mm working ports. For fetoscopic surgery, four 3 mm working ports (Storz Medical) were inserted into the uterus. Intra-amniotic insufflation was induced using warmed humidified CO_2 to 5–8 mm Hg working pressure. Probes were inserted into the fetal rectum for monitoring throughout the surgical procedures. The repair was completed by patch closure of the dura (Durepair, MedTronic) and primary closure of the skin with intermittent fetal echocardiography monitoring as the reference standard. After repair, hysterotomies were closed, and gestation was allowed to continue until killing at 125 days.

In vivo physiologic monitoring studies

Preoperatively, probes were sterilized via autoclave at 121 °C and 15 pounds per square inch for 30 min. The devices are used repeatedly and autoclaved each time, in the same fashion as surgical tools. The probe has one size for sheep with different fetal gestational ages, where the length is set as the longest one that can fit into the youngest fetus. These same probes also provide good signal quality for older fetuses because of the proximity of the vasculature and the rectum in fetuses with various gestational ages. If the distance between the sensor and the vessels increases substantially as the fetus grows, then the length of the probe should be increased (that is, a greater distance between the LEDs and PDs for probing deeper vessels) to ensure good signal quality. For the expanding balloon actuator, the same actuator can expand to 5 mm, sufficient to cover the range of rectum diameters at various fetal gestational ages for sensor securement.

During the experiments, an umbilical artery catheter with a three-way stopcock was placed for fetal ABG sampling. Fetal monitoring probes were inserted into the esophagus or rectum, depending on the experiment of interest. A minimum of 2 fetal ABGs (approximately 150 µl) were obtained over a span of 10 min for baseline data. Fetal umbilical ABGs were obtained throughout the duration of hypoxia experiments at approximately 3–5 min intervals and analysed using either i-STAT Alinity (Abbott Laboratories) or GEM Premier 5000 (Werfen) blood gas analysers. Continuous fetal echocardiography was performed using the EPIQ Elite ultrasound machine equipped with a C5-1 curved array ultrasound transducer (5–1 MHz, Philips Medical Systems) as a reference for FHR.

Maternal hypoxia, umbilical cord occlusion and fetal hypothermia experiments were performed between 90 and 125 days of gestation. For maternal hypoxia experiments, temporary cessation of respirations on the ventilator was performed. Propofol bolus was administered if any spontaneous breaths occurred. Maternal hypoxia was continued to a goal of 70–80% oxygen saturation or the onset of fetal bradycardia (FHR < 80), after which respirations were resumed, and the mother and fetus were allowed to recover. Multiple experiments were performed in each animal as tolerated, allowing for the return to maternal baseline SpO_2 and fetal baseline HR and SpO_2 in between events.

For umbilical cord occlusion experiments, silastic vessel loops (Medline) were placed around the umbilical cord and tightened until blanching was visualized in the umbilical vein, but palpable pulsatile flow was maintained within the umbilical artery. Preservation of umbilical artery flow was performed to simulate low levels of pressure that can induce cord occlusion from fetal mispositioning or intra-amniotic insufflation in fetoscopic surgery. Cord compression was maintained until fetal bradycardia (FHR < 80) developed, after which compression was released, and the fetus was allowed to recover to baseline FHR and SpO_2 in between events.

For fetal hypothermia experiments, an additional fetal nasal temperature probe was inserted for reference monitoring. Fetuses were exteriorized completely from the uterus for fetal cooling. After exteriorization, baseline readings were obtained after insertion of the SRFP and an esophageal veterinary temperature probe for approximately 10 min. Fetal hypothermia was induced with gradual wetting of the fetal skin with room-temperature (20–22 °C) saline. Fetal hypothermia was produced gradually to approximately 33 °C, and the fetus was subsequently rewarmed with warm saline (36–38 °C).

Physiologic monitoring studies concluded with either closure of the uterus and abdomen as described above and subsequent recovery in a postoperative recovery area, or sodium pentobarbital/sodium phenytoin euthanasia for non-survival surgeries. For survival experiments, postoperative behaviour and physiological function were carefully monitored to ensure complete recovery from anaesthesia, and they eventually returned to their primary enclosures. Ewes were fed Rumilab (LabDiet) pelleted diet and hay ad libitum. To control pain after surgery, meloxicam 0.5–1.0 mg kg^{-1} was administered daily for at least 72 h. Ewes were under veterinary surveillance and monitoring for signs of distress or breakthrough pain. Postoperative ultrasound was performed at 24 h and 48 h after each experiment apart from non-survival surgeries to confirm the presence of an FHR.

Data acquisition and processing

The sensors are paired with a customized BLE receiver dongle (NRF52832 evaluation board), which is connected to a tablet (Surface Pro, Microsoft) via USB. Custom Python code with Python 3.8.10 was used to receive data by BLE. Custom Python code with Python 3.8.10, Scipy 1.7.3, Numpy 1.20.2 and Matplotlib 3.3.4 was used to process, plot and save PPG, thermistor and ECG signals. MATLAB 2023a (MATHWORKS) was used for post-processing the recorded data, beginning with digital band-pass filtering using a Butterworth filter. The passband was set to 0.1–5 Hz for PPG and 1–35 Hz for ECG. Spectral analysis was conducted using short-time Fourier transform with a 10 s window and a 90% overlap, generating spectrograms that illustrated the time–frequency characteristics of each signal.

Fetal histology

Post-mortem examination of the fetal rectum occurred after use of the probe in the fetoscopic myelomeningocele repair validation experiments. On necropsy, the fetal rectum was dissected and stored in formalin for 48 h. Samples were transferred to 70% ethanol until further processing. The tissues were processed, embedded in paraffin wax and sectioned in 10 µm increments. Haematoxylin and eosin staining was performed.

Reporting summary

Further information on research design is available in the Nature Portfolio Reporting Summary linked to this article.

Data availability

Raw data generated during the current study are available from the corresponding authors on reasonable request. The analysed data

are available at https://doi.org/10.5281/zenodo.17371614 (ref. 71). Source data that support the findings of this study are included within this paper and its Supplementary Information files. Source data are provided with this paper.

Code availability

All computer code and customized software generated during and/or used in the current study are available at https://doi.org/10.5281/zenodo.17371614 (ref. 71).

References

1. CDC. Birth defects (2024); https://www.cdc.gov/birth-defects/data-research/facts-stats/index.html
2. Parker, S. E. et al. Updated national birth prevalence estimates for selected birth defects in the United States, 2004–2006. *Birth Defects Res. A Clin. Mol. Teratol.* **88**, 1008–1016 (2010).
3. Mai, C. T. et al. National population-based estimates for major birth defects, 2010–2014. *Birth Defects Res.* **111**, 1420–1435 (2019).
4. Wilson, R. D. In utero therapy for fetal thoracic abnormalities. *Prenat. Diagn.* **28**, 619–625 (2008).
5. Warner, L. L., Arendt, K. W., Ruano, R., Qureshi, M. Y. & Segura, L. G. A call for innovation in fetal monitoring during fetal surgery. *J. Matern.-Fetal Neonatal Med.* **35**, 1817–1823 (2022).
6. Pinas, A. & Chandraharan, E. Continuous cardiotocography during labour: analysis, classification and management. *Best Pract. Res. Clin. Obstet. Gynaecol.* **30**, 33–47 (2016).
7. Alfirevic, Z., Devane, D. & Gyte, G. M. Continuous cardiotocography (CTG) as a form of electronic fetal monitoring (EFM) for fetal assessment during labour. *Cochrane Database Syst. Rev.* https://doi.org/10.1002/14651858.cd006066.pub2 (2013).
8. Neilson, J. P. Fetal electrocardiogram (ECG) for fetal monitoring during labour. *Cochrane Database Syst. Rev.* **2015**, CD000116 (2015).
9. Symonds, E. M., Sahota, D. & Chang, A. *Fetal Electrocardiography*. Cardiopulmonary Medicine from Imperial College Press (Imperial College Press, 2001).
10. Behar, J. A. et al. Noninvasive fetal electrocardiography for the detection of fetal arrhythmias. *Prenat. Diagn.* **39**, 178–187 (2019).
11. Kahankova, R. et al. A review of recent advances and future developments in fetal phonocardiography. *IEEE Rev. Biomed. Eng.* **16**, 653–671 (2023).
12. Adithya, P. C., Sankar, R., Moreno, W. A. & Hart, S. Trends in fetal monitoring through phonocardiography: challenges and future directions. *Biomed. Signal Process. Control* **33**, 289–305 (2017).
13. Wacker-Gussmann, A., Strasburger, J. F. & Wakai, R. T. Contribution of fetal magnetocardiography to diagnosis, risk assessment, and treatment of fetal arrhythmia. *J. Am. Heart Assoc.* **11**, e025224 (2021).
14. Strasburger, J. F., Cheulkar, B. & Wakai, R. T. Magnetocardiography for fetal arrhythmias. *Heart Rhythm* **5**, 1073–1076 (2008).
15. Reuss, J. L. Factors influencing fetal pulse oximetry performance. *J. Clin. Monit. Comput.* **18**, 13–24 (2004).
16. East, C. E., Begg, L., Colditz, P. B. & Lau, R. Fetal pulse oximetry for fetal assessment in labour. *Cochrane Database Syst. Rev.* **2014**, CD004075 (2014).
17. Donofrio, M. T. et al. Diagnosis and treatment of fetal cardiac disease. *Circulation* **129**, 2183–2242 (2014).
18. Strasburger, J. F. & Wakai, R. T. Fetal cardiac arrhythmia detection and in utero therapy. *Nat. Rev. Cardiol.* **7**, 277–290 (2010).
19. Engwall-Gill, A. J. & Perrone, E. E. in *Pediatric Surgery* (eds Coppola, C. P. et al.) 263–272 (Springer, 2022).
20. Kohl, T. Minimally invasive fetoscopic interventions: an overview in 2010. *Surg. Endosc.* **24**, 2056–2067 (2010).
21. Ouyang, W. et al. A wireless and battery-less implant for multimodal closed-loop neuromodulation in small animals. *Nat. Biomed. Eng.* **7**, 1252–1269 (2023).
22. McCall, J. G. et al. Fabrication and application of flexible, multimodal light-emitting devices for wireless optogenetics. *Nat. Protoc.* **8**, 2413–2428 (2013).
23. Gutruf, P. et al. Fully implantable optoelectronic systems for battery-free, multimodal operation in neuroscience research. *Nat. Electron.* **1**, 652–660 (2018).
24. Cianchetti, M., Laschi, C., Menciassi, A. & Dario, P. Biomedical applications of soft robotics. *Nat. Rev. Mater.* **3**, 143–153 (2018).
25. Konishi, S., Kobayashi, T., Maeda, H., Asajima, S. & Makikawa, M. Cuff actuator for adaptive holding condition around nerves. *Sens. Actuators B* **83**, 60–66 (2002).
26. Runciman, M., Darzi, A. & Mylonas, G. P. Soft robotics in minimally invasive surgery. *Soft Robot.* **6**, 423–443 (2019).
27. Kim, Y., Parada, G. A., Liu, S. & Zhao, X. Ferromagnetic soft continuum robots. *Sci. Robot.* **4**, 33 (2019).
28. Marechal, L. et al. Toward a common framework and database of materials for soft robotics. *Soft Robot.* **8**, 284–297 (2021).
29. Zhang, Y., Liao, J., Chen, M., Li, X. & Jin, G. A multi-module soft robotic arm with soft actuator for minimally invasive surgery. *Int. J. Med. Robot. Comput. Assist. Surg.* **19**, e2467 (2023).
30. Coutrot, M. et al. Perfusion index: physical principles, physiological meanings and clinical implications in anaesthesia and critical care. *Anaesth. Crit. Care Pain Med.* **40**, 100964 (2021).
31. Elgendi, M. Optimal signal quality index for photoplethysmogram signals. *Bioengineering* **3**, 21 (2016).
32. McCauley, M. D. & Wehrens, X. H. T. Ambulatory ECG recording in mice. *J. Vis. Exp.* https://doi.org/10.3791/1739 (2010).
33. Fenske, S. et al. Comprehensive multilevel in vivo and in vitro analysis of heart rate fluctuations in mice by ECG telemetry and electrophysiology. *Nat. Protoc.* **11**, 61–86 (2016).
34. Hennis, K. et al. In vivo and ex vivo electrophysiological study of the mouse heart to characterize the cardiac conduction system, including atrial and ventricular vulnerability. *Nat. Protoc.* **17**, 1189–1222 (2022).
35. Chehbani, A., Sahuguede, S., Julien-Vergonjanne, A. & Bernard, O. Quality indexes of the ECG signal transmitted using optical wireless link. *Sensors* **23**, 4522 (2023).
36. Rahman, S., Karmakar, C., Natgunanathan, I., Yearwood, J. & Palaniswami, M. Robustness of electrocardiogram signal quality indices. *J. R. Soc. Interface* **19**, 20220012 (2022).
37. Wang, Y., Qu, Z., Wang, W. & Yu, D. PVA/CMC/PEDOT:PSS mixture hydrogels with high response and low impedance electronic signals for ECG monitoring. *Colloids Surf. B* **208**, 112088 (2021).
38. Versek, C., Frasca, T., Zhou, J., Chowdhury, K. & Sridhar, S. Electric field encephalography for brain activity monitoring. *J. Neural Eng.* **15**, 046027 (2018).
39. Rosell, J., Colominas, J., Riu, P., Pallas-Areny, R. & Webster, J. G. Skin impedance from 1 Hz to 1 MHz. *IEEE Trans. Biomed. Eng.* **35**, 649–651 (1988).
40. Goyal, K., Borkholder, D. A. & Day, S. W. Dependence of skin-electrode contact impedance on material and skin hydration. *Sensors* **22**, 8510 (2022).
41. Lee, S. Y. et al. Evolution and variations of the ovine model of spina bifida. *Fetal Diagn. Ther.* **50**, 491–500 (2023).
42. Rosén, K. G., Hökegård, K. H. & Kjellmer, I. A study of the relationship between the electrocardiogram and hemodynamics in the fetal lamb during asphyxia. *Acta Physiol. Scand.* **98**, 275–284 (1976).
43. Westgate, J. A. et al. Do fetal electrocardiogram PR-RR changes reflect progressive asphyxia after repeated umbilical cord occlusion in fetal sheep? *Pediatr. Res.* **44**, 297–303 (1998).

44. Marwan, A. & Crombleholme, T. M. The EXIT procedure: principles, pitfalls, and progress. *Semin. Pediatr. Surg.* **15**, 107–115 (2006).
45. Spiers, A., Legendre, G., Biquard, F., Descamps, P. & Corroenne, R. Ex utero intrapartum technique (EXIT): indications, procedure methods and materno-fetal complications—a literature review. *J. Gynecol. Obstet. Hum. Reprod.* **51**, 102252 (2022).
46. Chen, G., Zhu, Z., Liu, J. & Wei, W. Esophageal pulse oximetry is more accurate and detects hypoxemia earlier than conventional pulse oximetry during general anesthesia. *Front. Med.* **6**, 406–410 (2012).
47. Phillips, J. P., Kyriacou, P. A., Jones, D. P., Shelley, K. H. & Langford, R. M. Pulse oximetry and photoplethysmographic waveform analysis of the esophagus and bowel. *Curr. Opin. Anesthesiol.* **21**, 779 (2008).
48. Varcoe, T. J. et al. Fetal cardiovascular response to acute hypoxia during maternal anesthesia. *Physiol. Rep.* **8**, e14365 (2020).
49. Fong, D. D. et al. Validation of a novel transabdominal fetal oximeter in a hypoxic fetal lamb model. *Reprod. Sci.* **27**, 1960–1966 (2020).
50. Park, J., Seok, H. S., Kim, S.-S. & Shin, H. Photoplethysmogram analysis and applications: an integrative review. *Front. Physiol.* **12**, 808451 (2022).
51. Elgendi, M. On the analysis of fingertip photoplethysmogram signals. *Curr. Cardiol. Rev.* **8**, 14–25 (2012).
52. Abushouk, A. et al. The dicrotic notch: mechanisms, characteristics, and clinical correlations. *Curr. Cardiol. Rep.* **25**, 807–816 (2023).
53. Inoue, N. et al. Second derivative of the finger photoplethysmogram and cardiovascular mortality in middle-aged and elderly Japanese women. *Hypertens. Res.* **40**, 207–211 (2017).
54. Hashimoto, J. et al. Pulse wave velocity and the second derivative of the finger photoplethysmogram in treated hypertensive patients: their relationship and associating factors. *J. Hypertens.* **20**, 2415–2422 (2022).
55. Street, P., Dawes, G. S., Moulden, M. & Redman, C. W. G. Short-term variation in abnormal antenatal fetal heart rate records. *Am. J. Obstet. Gynecol.* **165**, 515–523 (1991).
56. Young, B. K., Katz, M. & Wilson, S. J. Sinusoidal fetal heart rate. I. Clinical significance. *Am. J. Obstet. Gynecol.* **136**, 587–593 (1980).
57. Partridge, E. A. et al. An extra-uterine system to physiologically support the extreme premature lamb. *Nat. Commun.* **8**, 15112 (2017).
58. Kabagambe, S. K. et al. Lessons from the barn to the operating suite: a comprehensive review of animal models for fetal surgery. *Annu. Rev. Anim. Biosci.* **6**, 1–21 (2017).
59. Petersen, R., Connelly, A., Martin, S. L. & Kupper, L. L. Preventive counseling during prenatal care: Pregnancy Risk Assessment Monitoring System (PRAMS). *Obstet. Gynecol. Surv.* **56**, 599–601 (2001).
60. Veena, S. & Aravindhar, D. J. Remote monitoring system for the detection of prenatal risk in a pregnant woman. *Wirel. Pers. Commun.* **119**, 1051–1064 (2021).
61. Haga, Y. et al. Small diameter hydraulic active bending catheter using laser processed super elastic alloy and silicone rubber tube. In *2005 3rd IEEE/EMBS Special Topic Conference on Microtechnology in Medicine and Biology* 245–248 (2005).
62. Liao, Z. et al. On the stress recovery behaviour of Ecoflex silicone rubbers. *Int. J. Mech. Sci.* **206**, 106624 (2021).
63. Fung, Y.-C. in *Biomechanics: Mechanical Properties of Living Tissues* 321–391 (Springer, 1993).
64. Fang, Q. & Boas, D. A. Monte Carlo simulation of photon migration in 3D turbid media accelerated by graphics processing units. *Opt. Express* **17**, 20178–20190 (2009).
65. Yu, L., Nina-Paravecino, F., Kaeli, D. & Fang, Q. Scalable and massively parallel Monte Carlo photon transport simulations for heterogeneous computing platforms. *J. Biomed. Opt.* **23**, 010504–010504 (2018).
66. Lu, W. et al. Wireless, implantable catheter-type oximeter designed for cardiac oxygen saturation. *Sci. Adv.* **7**, eabe0579 (2021).
67. Bosschaart, N., Edelman, G. J., Aalders, M. C. G., Leeuwen, T. G. V. & Faber, D. J. A literature review and novel theoretical approach on the optical properties of whole blood. *Lasers Med. Sci.* **29**, 453–479 (2014).
68. Khan, R., Gul, B., Khan, S., Nisar, H. & Ahmad, I. Refractive index of biological tissues: review, measurement techniques, and applications. *Photodiagnosis Photodyn. Ther.* **33**, 102192 (2021).
69. Morrison, J. L. et al. Improving pregnancy outcomes in humans through studies in sheep. *Am. J. Physiol. Regul. Integr. Comp. Physiol.* **315**, R1123–R1153 (2018).
70. Joyeux, L. et al. Validation of the fetal lamb model of spina bifida. *Sci. Rep.* **9**, 9327 (2019).
71. Zhou, J. et al. Data and code for the article 'A filamentary soft robotic probe for multimodal in utero monitoring of fetal health'. *Zenodo* https://doi.org/10.5281/zenodo.17371614 (2025).

Acknowledgements

This work was funded by the Querrey-Simpson Institute for Bioelectronics. In vivo studies were supported by the Ann & Robert H. Lurie Children's Hospital Foundation. This work made use of the NUFAB facility of Northwestern University's NUANCE Center, which has received support from the SHyNE Resource (NSF ECCS-2025633), the IIN and Northwestern's MRSEC programme (NSF DMR-2308691). The funders had no role in study design, data collection and analysis, decision to publish or preparation of the paper.

Author contributions

Conceptualization: H.B., J.Z., A.F.S. and J.A.R. Methodology: H.B., J.Z., S. Papastefan, X.L., A.F.S. and J.A.R. Theoretical simulations: X.L., H.Z. and Y.H. Investigation: H.B., J.Z., M.W., S. Papastefan, X.L., K.Z., Z.Z., W.O., C.R.R., A.M.A., H.W., Y.Z., K. Madsen, S.L., A.I.E., K. Ma, L.K., S. Patel, D.R.L., K.C.O., R.G., S.S., W.Z. and A.F.S. Software: J.Z. and W.O. Formal analysis: H.B., J.Z. and S. Papastefan. Validation: H.B., J.Z. and S. Papastefan. Data curation: H.B., J.Z., M.W. and S. Papastefan. Visualization: M.W., H.B., J.Z., S. Papastefan and X.L. Supervision: Y.H., A.F.S. and J.A.R. Funding acquisition: A.F.S. and J.A.R. Writing (original draft): H.B., J.Z., S. Papastefan and X.L. Writing (review and editing): J.Z., M.W., H.B., S. Papastefan, X.L., A.F.S. and J.A.R. H.B., J.Z., M.W., S. Papastefan and X.L. contributed equally to this work.

Competing interests

The authors declare no competing interests.

Additional information

Extended data is available for this paper at https://doi.org/10.1038/s41551-025-01605-3.

Supplementary information The online version contains supplementary material available at https://doi.org/10.1038/s41551-025-01605-3.

Correspondence and requests for materials should be addressed to Hedan Bai, Yonggang Huang, Aimen F. Shaaban or John A. Rogers.

Peer review information *Nature Biomedical Engineering* thanks Anna David, Ellen Roche and the other, anonymous, reviewer(s) for their contribution to the peer review of this work.

Reprints and permissions information is available at www.nature.com/reprints.

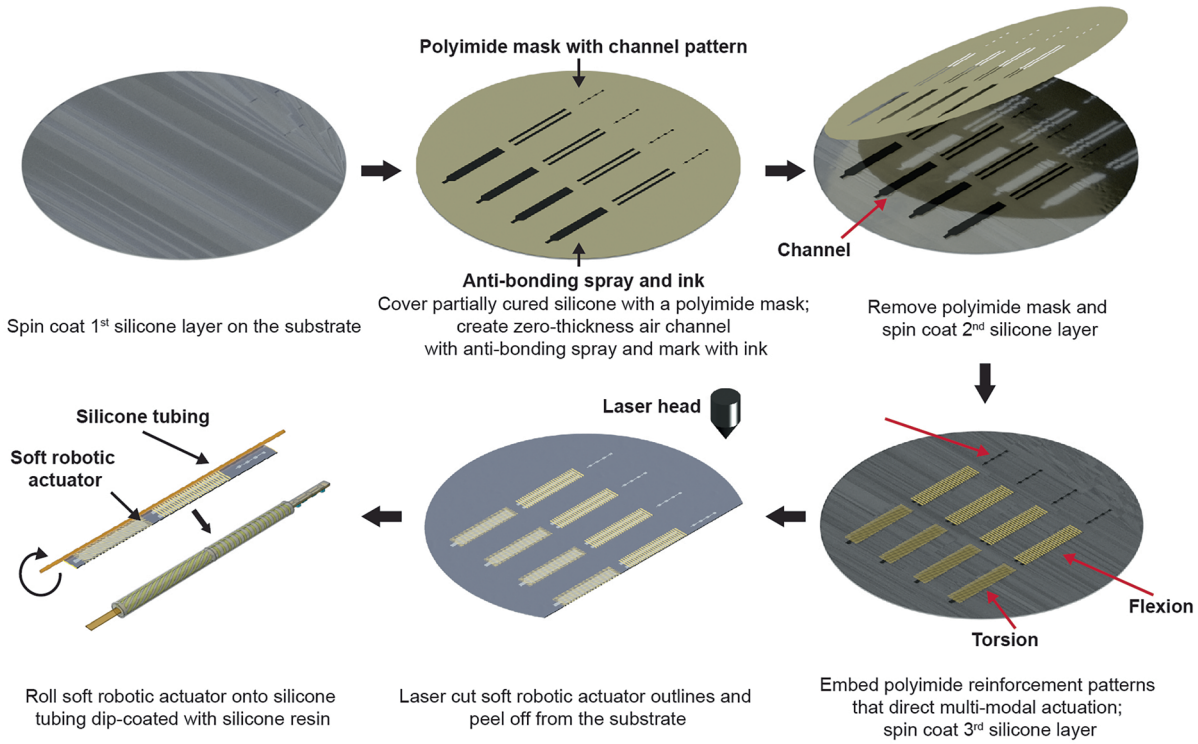
Publisher's note Springer Nature remains neutral with regard to jurisdictional claims in published maps and institutional affiliations.

Springer Nature or its licensor (e.g. a society or other partner) holds exclusive rights to this article under a publishing agreement with the author(s) or other rightsholder(s); author self-archiving of the accepted manuscript version of this article is solely governed by the terms of such publishing agreement and applicable law.

© The Author(s), under exclusive licence to Springer Nature Limited 2026

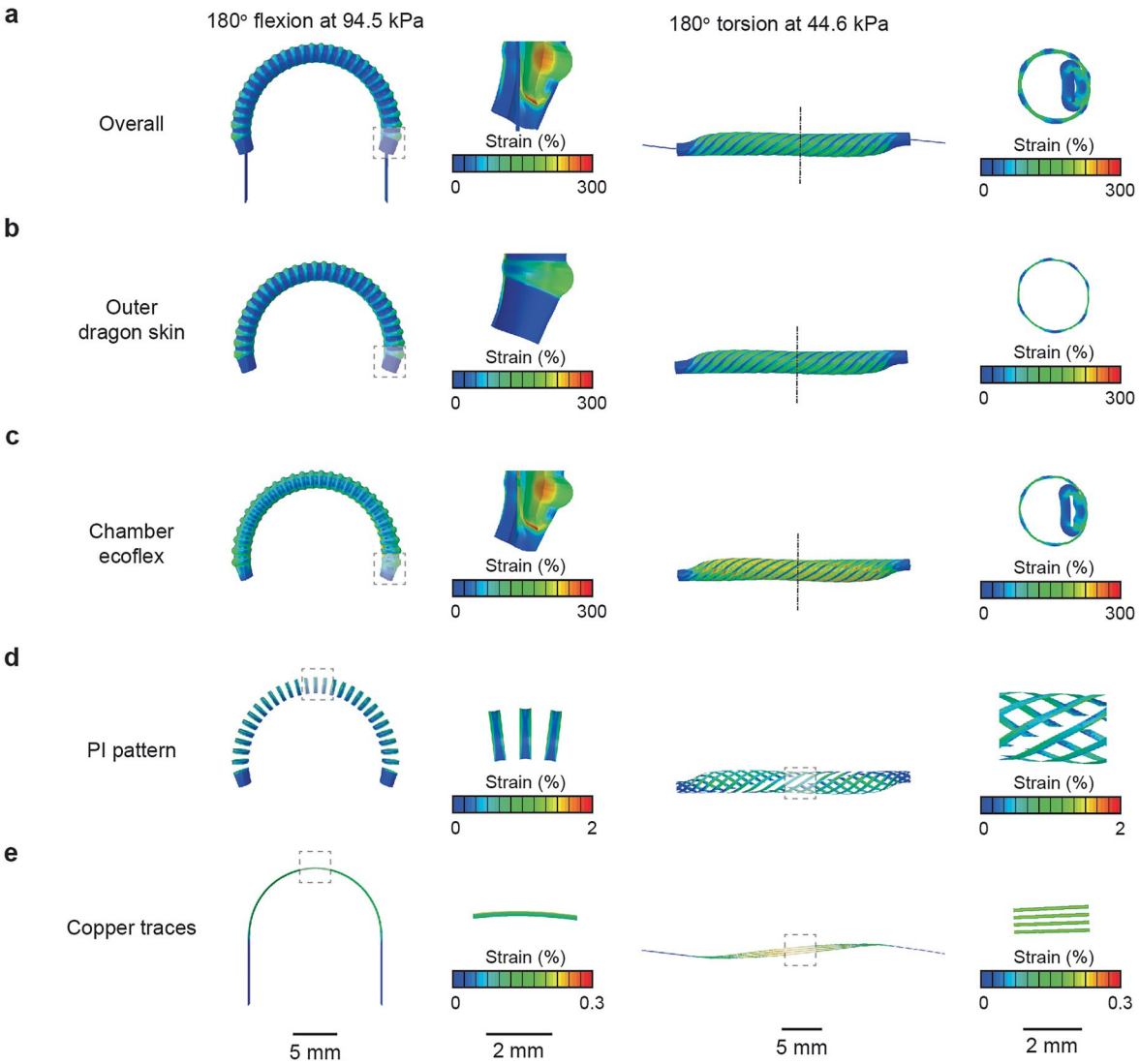
[1]Querrey Simpson Institute for Bioelectronics, Northwestern University, Evanston, IL, USA. [2]Department of Materials, ETH Zurich, Zurich, Switzerland. [3]The Chicago Institute for Fetal Health, Ann & Robert H. Lurie Children's Hospital of Chicago, Chicago, IL, USA. [4]Division of Pediatric Surgery, Department of Surgery, Feinberg School of Medicine, Northwestern University, Chicago, IL, USA. [5]Department of Civil and Environmental Engineering, Northwestern University, Evanston, IL, USA. [6]State Key Laboratory of Mechanical System and Vibration, School of Mechanical Engineering, Shanghai Jiao Tong University, Shanghai, China. [7]Department of Materials Science and Engineering, Northwestern University, Evanston, IL, USA. [8]Department of Mechanical Engineering, Northwestern University, Evanston, IL, USA. [9]Department of Electrical and Computer Engineering, Northwestern University, Evanston, IL, USA. [10]Department of Chemistry, University of Illinois at Urbana-Champaign, Urbana, IL, USA. [11]Department of Biomedical Engineering, Northwestern University, Evanston, IL, USA. [12]Department of Neuroscience, Feinberg School of Medicine, Northwestern University, Chicago, IL, USA. [13]Department of Systems Engineering and Industrial Technologies, University of Parma, Parma, Italy. [14]Department of Radiology, Pritzker School of Medicine, University of Chicago, Chicago, IL, USA. [15]Center for Bio-Integrated Electronics, Northwestern University, Evanston, IL, USA. [16]Department of Neurological Surgery, Feinberg School of Medicine, Northwestern University, Chicago, IL, USA. [17]These authors contributed equally: Hedan Bai, Jianlin Zhou, Mingzheng Wu, Steven Papastefan, Xiuyuan Li. ✉e-mail: hedan.bai@mat.ethz.ch; y-huang@northwestern.edu; ashaaban@luriechildrens.org; jrogers@northwestern.edu

https://doi.org/10.1038/s41551-025-01605-3



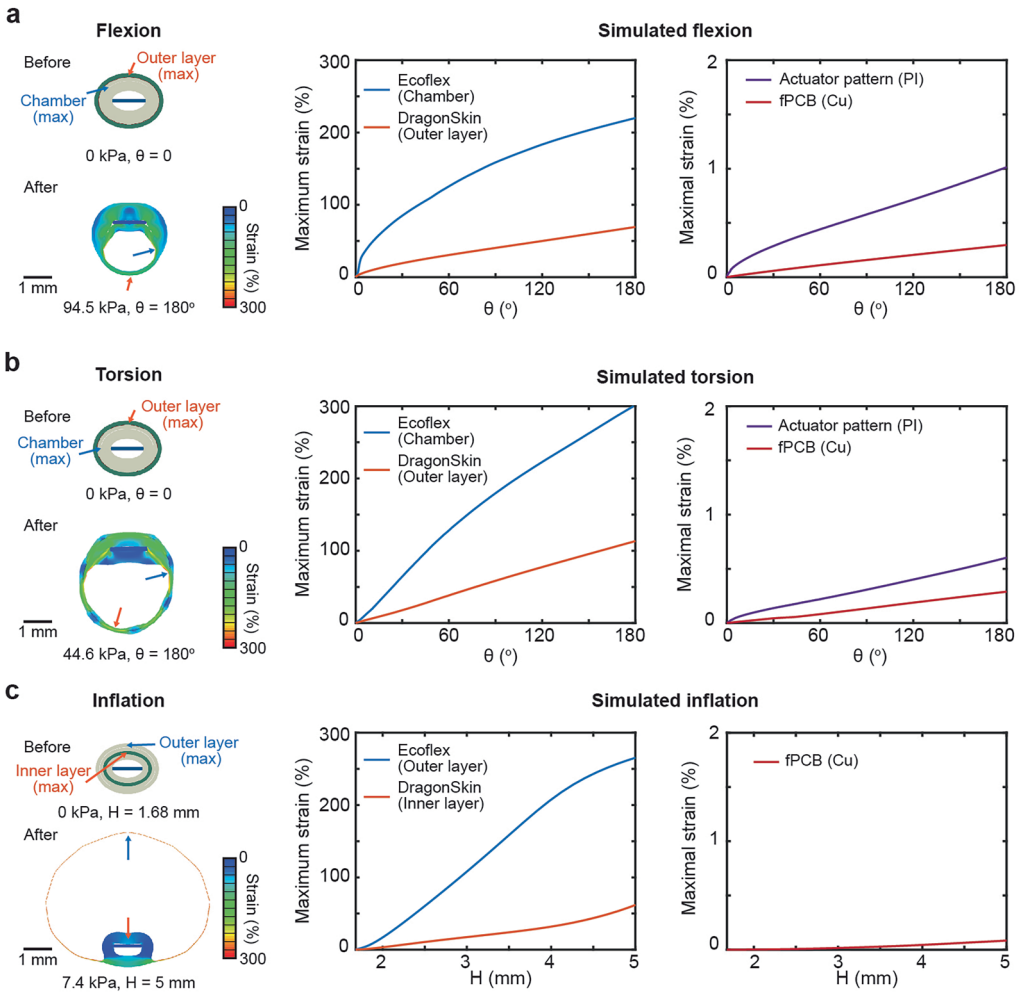
Extended Data Fig. 1 | Fabrication procedures of the 3D soft robotic actuator.

https://doi.org/10.1038/s41551-025-01605-3



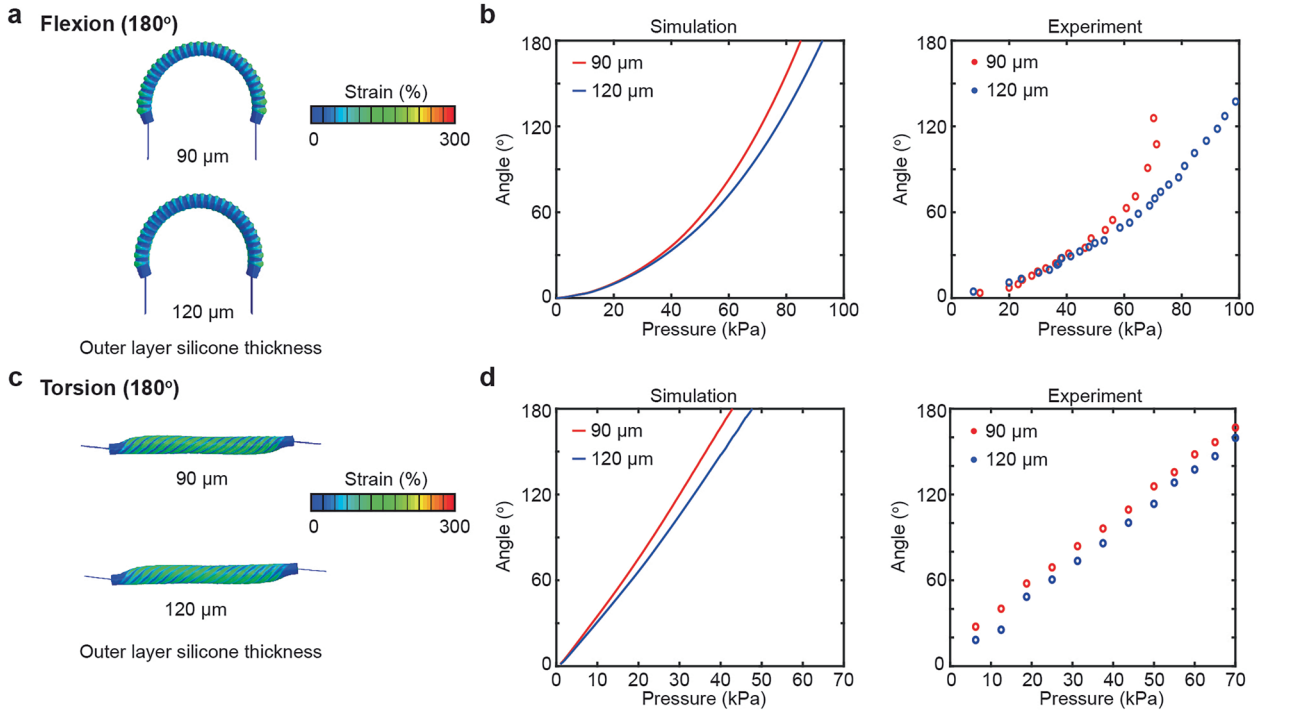
Extended Data Fig. 2 | Finite element analysis of strain distribution on actuator layers. (**a**) Overall strain distribution. (**b**) Strain distribution on the outer outer tear-resistant platinum-cure silicone elastomer (for example, DragonSkin-type, Smooth-On, Inc) layer. (**c**) Strain distribution on the low-modulus platinum-cure silicone (for example, Ecoflex-type, Smooth-On, Inc) chamber with enlarged views of critical edge leading to failure. (**d**) Strain distribution on polyimide strain limiting patterns. (**e**) Strain distribution on the copper layer of the probe.

https://doi.org/10.1038/s41551-025-01605-3



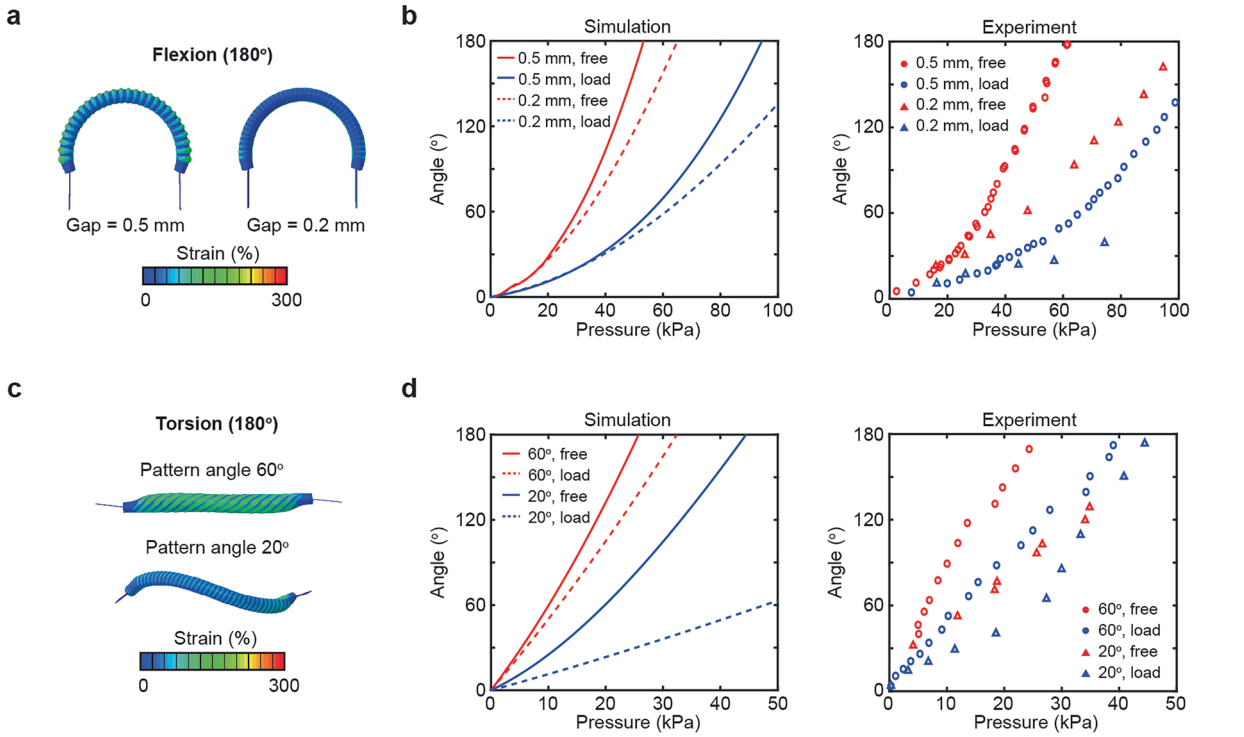
Extended Data Fig. 3 | Maximum strain on soft robotic structures during actuation. (**a**) Left, FEA results showing cross-sectional strain distribution profile of silicone layers before and after flexion actuation. Scale bar, 1 mm. Arrows indicate the maximum strain points at the outer layer (orange) and chamber layer (blue). Right, maximum strain on different structures relative to the flexion angle. (**b**) Same as (**a**) but for torsion. (**c**) Same as (**a**) but for balloon inflation and inflation height.

https://doi.org/10.1038/s41551-025-01605-3



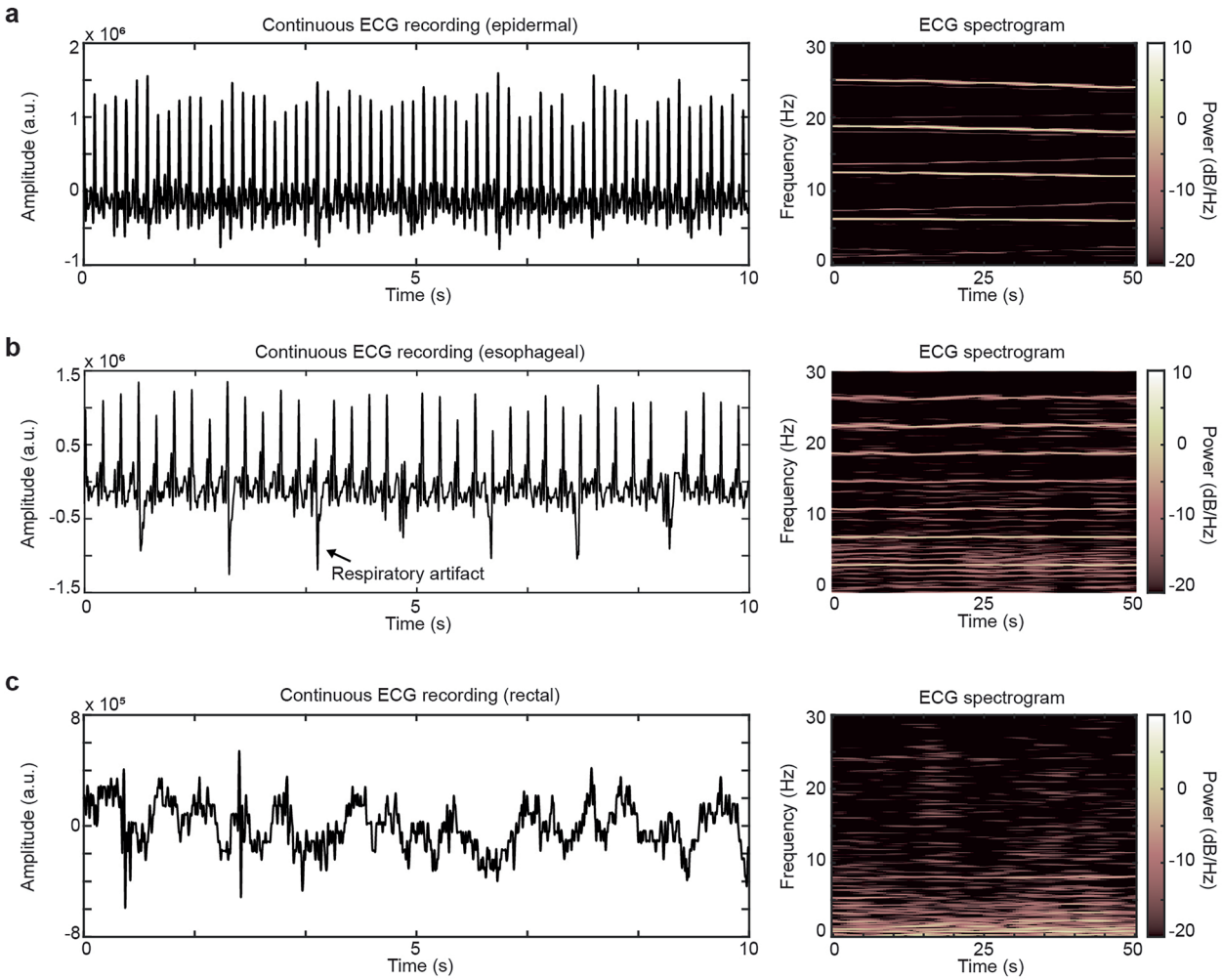
Extended Data Fig. 4 | Optimization of the outer layer thickness of the soft robotic actuator. (**a**) Strain contour of flexion actuator with different outer layer thickness at a 180° flexion angle. (**b**) Simulation and experimental results of flexion angle with different outer layer thicknesses. (**c**) Strain contour of torsion actuator with different outer layer thickness at a 180° torsion angle. (**d**) Simulation and experiment result of torsion angle with different outer layer thickness. 120 μm, same data as load in Fig. 2d.

https://doi.org/10.1038/s41551-025-01605-3



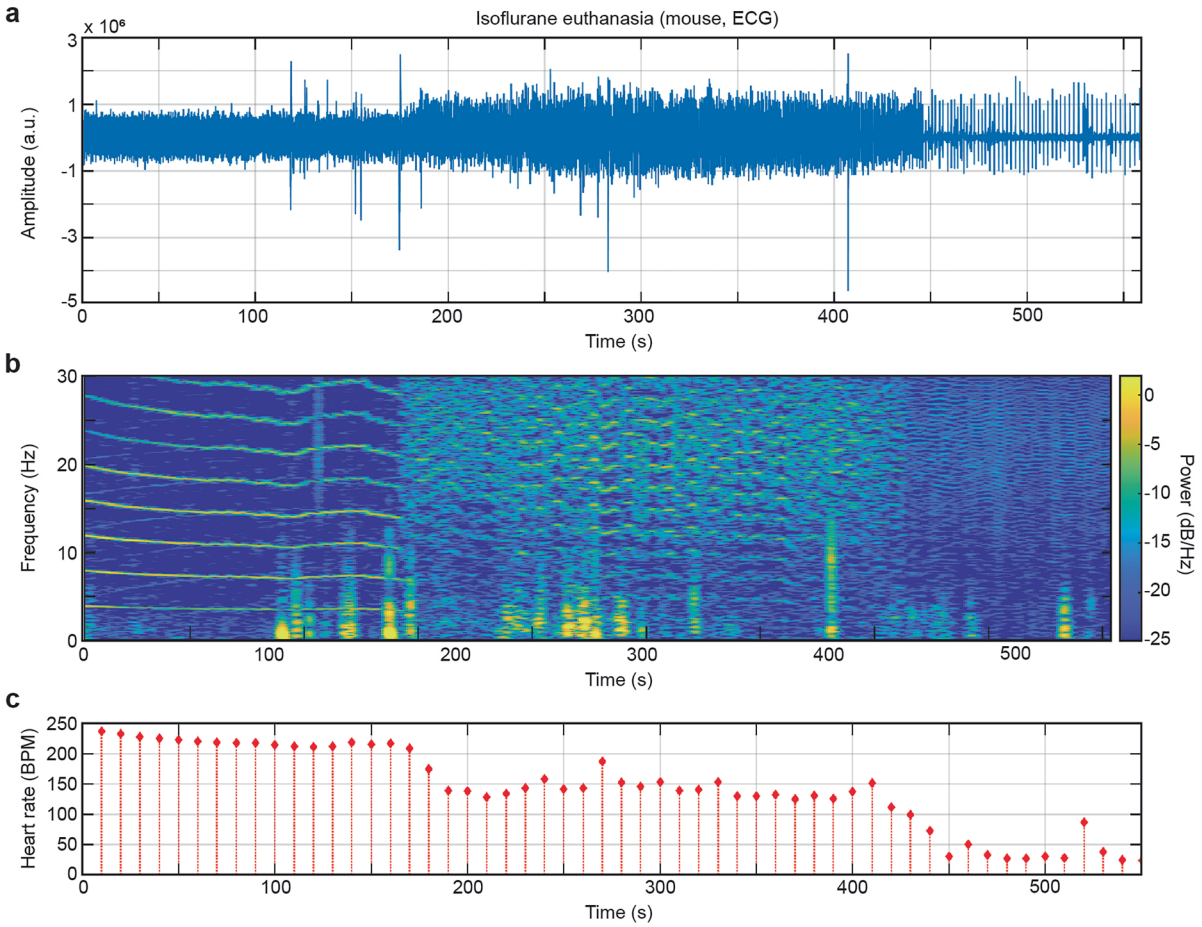
Extended Data Fig. 5 | Numerical and experimental characterization of multimodal soft robotic actuator patterns. (**a**) Strain contour of flexion actuator with different pattern gap widths at a 180° flexion angle. (**b**) Simulation and experimental results of flexion angle with different pattern gap width. (**c**) Strain contour of torsion actuator with different pattern angles at a 180° torsion angle. (**d**) Simulation and experimental results of torsion angle with different pattern angles.

https://doi.org/10.1038/s41551-025-01605-3



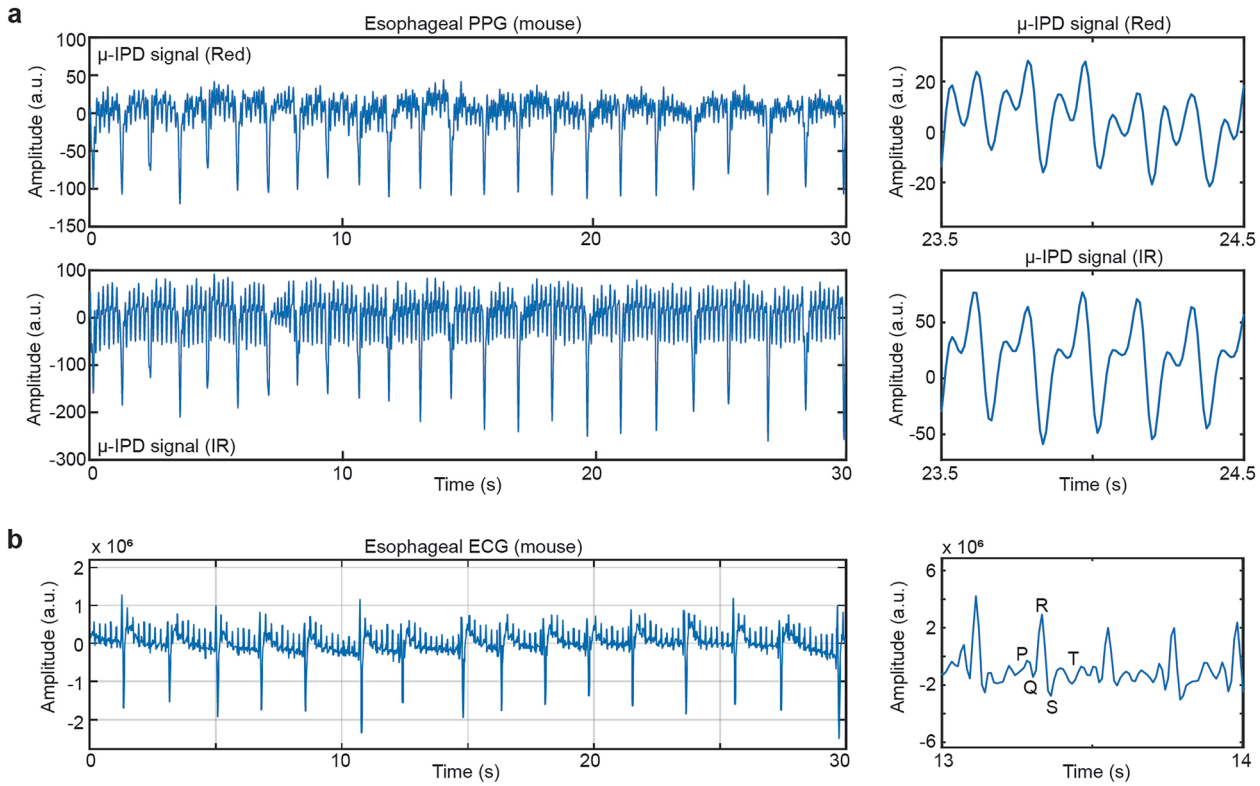
Extended Data Fig. 6 | ECG characteristics with different deployment approaches. (**a**) Waveform and frequency spectrogram of ECG signal recorded from an adult mouse using SRFP with an epidermal approach. (**b**) Same as (**a**), but for the esophageal approach. (**c**) Same as (**a**), but for the rectal approach.

https://doi.org/10.1038/s41551-025-01605-3



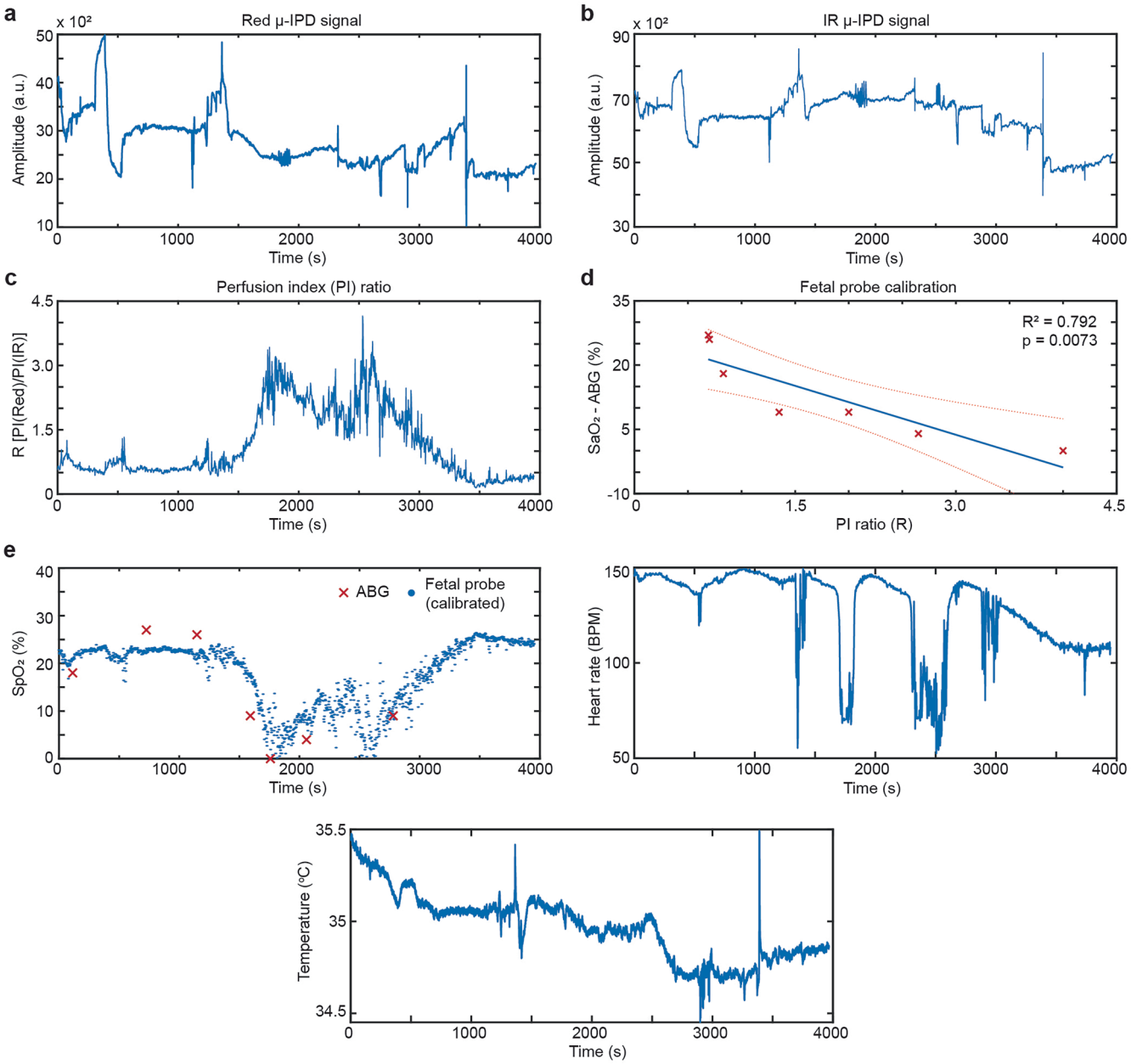
Extended Data Fig. 7 | Validation of ECG signal detection in response to isoflurane euthanasia. (**a**) Raw continuous ECG signals recorded during isoflurane euthanasia of an adult mouse using SRFP. (**b**) Frequency spectrum of recorded ECG signals during isoflurane euthanasia. (**c**) Calculated heart rate during isoflurane euthanasia.

https://doi.org/10.1038/s41551-025-01605-3



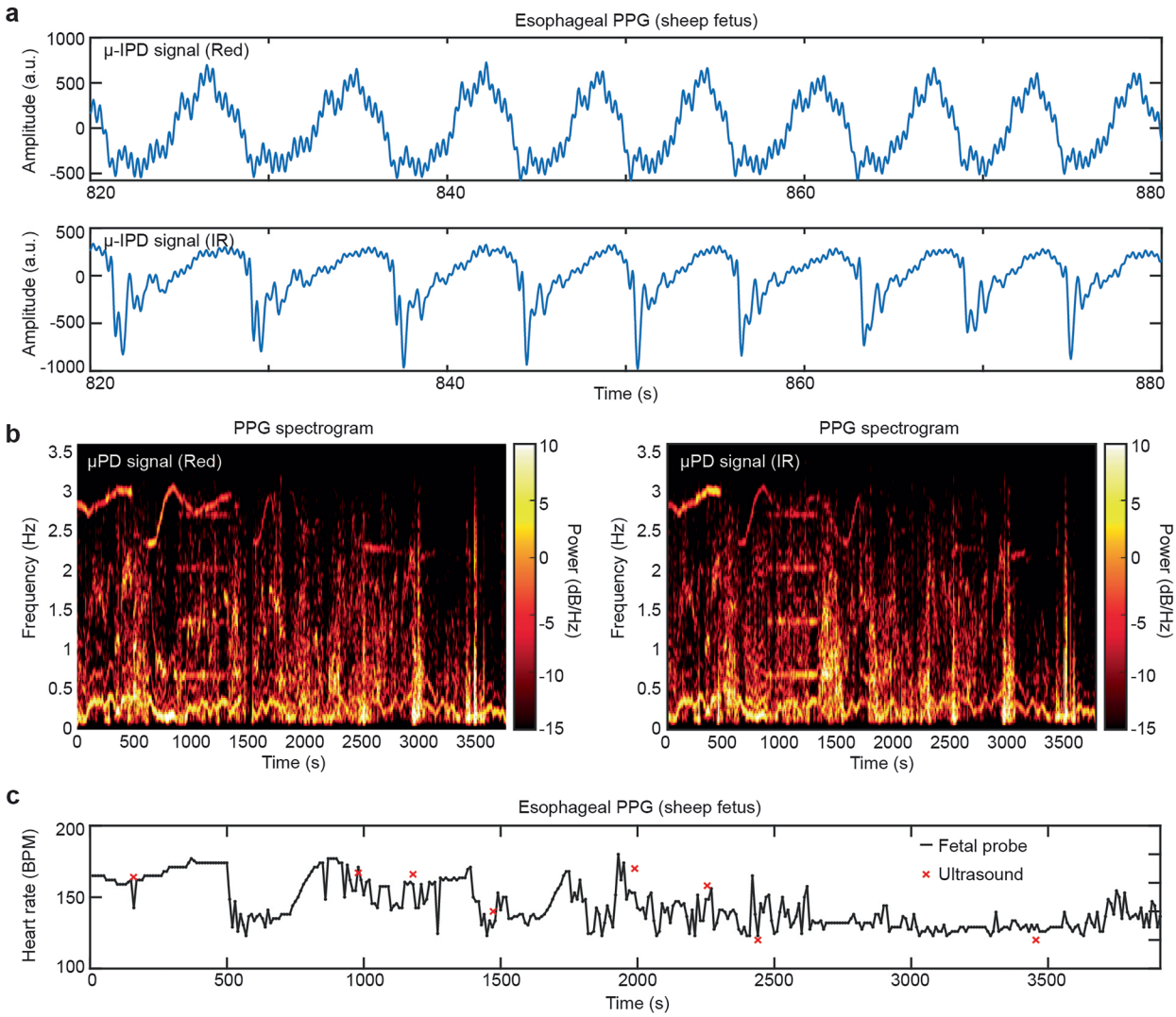
Extended Data Fig. 8 | Esophageal approach for physiological monitoring in a mouse model. (**a**) Raw μ-IPD (Red and IR) signals showing esophageal PPG waveform recorded from an adult mouse. (**b**) Raw electrical signals showing esophageal ECG waveform recorded from an adult mouse.

https://doi.org/10.1038/s41551-025-01605-3



Extended Data Fig. 9 | Calibration of fetal SpO_2 with cord blood gas analysis. (**a-b**) Raw continuous μ-IPD signals during an ex-utero sheep fetal surgery. (**c**) The ratio R between the perfusion indices of red and IR μ-IPD signals. (**d**) Calibration of fetal SpO_2 using linear regression between the perfusion index ratio R and arterial blood gas SaO_2 values. (**e**) Computed physiological parameters, including calibrated SpO_2, heart rate, and core temperature, during the same period of the experiment.

https://doi.org/10.1038/s41551-025-01605-3



Extended Data Fig. 10 | Esophageal approach for physiological monitoring during ex utero intrapartum treatment. (**a**) Raw μ-IPD (Red and IR) signals showing the esophageal PPG waveform recorded from a sheep fetus. (**b**) PPG spectrogram (Red and IR) showing the esophageal PPG frequency recorded from a sheep fetus. (**c**) Calculated heart rate from esophageal PPG recording of a sheep fetus.

nature portfolio

Corresponding author(s): John A. Rogers

Last updated by author(s): Oct 15, 2025

Reporting Summary

Nature Portfolio wishes to improve the reproducibility of the work that we publish. This form provides structure for consistency and transparency in reporting. For further information on Nature Portfolio policies, see our Editorial Policies and the Editorial Policy Checklist.

Statistics

For all statistical analyses, confirm that the following items are present in the figure legend, table legend, main text, or Methods section.

n/a	Confirmed	
☐	☒	The exact sample size (*n*) for each experimental group/condition, given as a discrete number and unit of measurement
☐	☒	A statement on whether measurements were taken from distinct samples or whether the same sample was measured repeatedly
☐	☒	The statistical test(s) used AND whether they are one- or two-sided *Only common tests should be described solely by name; describe more complex techniques in the Methods section.*
☐	☒	A description of all covariates tested
☐	☒	A description of any assumptions or corrections, such as tests of normality and adjustment for multiple comparisons
☐	☒	A full description of the statistical parameters including central tendency (e.g. means) or other basic estimates (e.g. regression coefficient) AND variation (e.g. standard deviation) or associated estimates of uncertainty (e.g. confidence intervals)
☐	☒	For null hypothesis testing, the test statistic (e.g. *F*, *t*, *r*) with confidence intervals, effect sizes, degrees of freedom and *P* value noted *Give P values as exact values whenever suitable.*
☒	☐	For Bayesian analysis, information on the choice of priors and Markov chain Monte Carlo settings
☒	☐	For hierarchical and complex designs, identification of the appropriate level for tests and full reporting of outcomes
☒	☐	Estimates of effect sizes (e.g. Cohen's *d*, Pearson's *r*), indicating how they were calculated

Our web collection on statistics for biologists contains articles on many of the points above.

Software and code

Policy information about availability of computer code

Data collection	Custom Python code with Python 3.8.10 was used to receive data by BLE.
Data analysis	Custom Python code with Python 3.8.10, Scipy 1.7.3, Numpy 1.20.2 and Matplotlib 3.3.4 was used to process, plot and save PPG, thermistor and ECG signals. MATLAB 2023a (MATHWORKS) was employed for post-processing the recorded data. All computer code and customized software generated during and/or used in the current study are available at https://doi.org/10.5281/zenodo.17371614.

For manuscripts utilizing custom algorithms or software that are central to the research but not yet described in published literature, software must be made available to editors and reviewers. We strongly encourage code deposition in a community repository (e.g. GitHub). See the Nature Portfolio guidelines for submitting code & software for further information.

Data

Policy information about availability of data

All manuscripts must include a data availability statement. This statement should provide the following information, where applicable:

- Accession codes, unique identifiers, or web links for publicly available datasets
- A description of any restrictions on data availability
- For clinical datasets or third party data, please ensure that the statement adheres to our policy

Raw data generated during the current study are available from the corresponding author on reasonable request. The analyzed data are available at https://doi.org/10.5281/zenodo.17371614. Source data that support the findings of this study are included within this paper and its Supplementary Information files.

Research involving human participants, their data, or biological material

Policy information about studies with human participants or human data. See also policy information about sex, gender (identity/presentation), and sexual orientation and race, ethnicity and racism.

Reporting on sex and gender	Sex and gender were not considered in this manuscript.
Reporting on race, ethnicity, or other socially relevant groupings	Neither race nor ethnicity was considered in this manuscript.
Population characteristics	The ages of individual participants were reported in the paper (ages 20-35).
Recruitment	Healthy normal subjects were recruited randomly from the Northwestern University campus in Evanston, IL, USA.
Ethics oversight	Institutional Review Board, Northwestern University (STU00220375).

Note that full information on the approval of the study protocol must also be provided in the manuscript.

Field-specific reporting

Please select the one below that is the best fit for your research. If you are not sure, read the appropriate sections before making your selection.

☒ Life sciences ☐ Behavioural & social sciences ☐ Ecological, evolutionary & environmental sciences

For a reference copy of the document with all sections, see nature.com/documents/nr-reporting-summary-flat.pdf

Life sciences study design

All studies must disclose on these points even when the disclosure is negative.

Sample size	Required sample sizes were estimated based on previous report of published results and our past experience performing similar experiments. No statistical methods were used to pre-determine sample sizes but our sample sizes are similar to those reported in previous publications.
Data exclusions	Data from failed samples were excluded from the analysis.
Replication	The number of replicates for each experiment were reported in the paper and the method section. All experiments were repeated at least twice. All attempts at replication were successful.
Randomization	Animals were randomly assigned to treatment groups. All samples were randomly assigned to experimental groups.
Blinding	Blinding was not relevant to the study, as no hypothesis-driven comparisons were performed in the study.

Reporting for specific materials, systems and methods

We require information from authors about some types of materials, experimental systems and methods used in many studies. Here, indicate whether each material, system or method listed is relevant to your study. If you are not sure if a list item applies to your research, read the appropriate section before selecting a response.

Materials & experimental systems

n/a	Involved in the study
☒	☐ Antibodies
☒	☐ Eukaryotic cell lines
☒	☐ Palaeontology and archaeology
☐	☒ Animals and other organisms
☒	☐ Clinical data
☒	☐ Dual use research of concern
☒	☐ Plants

Methods

n/a	Involved in the study
☒	☐ ChIP-seq
☒	☐ Flow cytometry
☒	☐ MRI-based neuroimaging

Animals and other research organisms

Policy information about studies involving animals; ARRIVE guidelines recommended for reporting animal research, and Sex and Gender in Research

Laboratory animals	The study involved wild-type C57BL/6 mice, obtained from Charles River (Wilmington, MA) and bred internally. Both adult male and female mice, aged 80 to 120 days, were included. Prior to procedures, all mice were group housed, maintained at approximately 25° C, 30 – 70% humidity, and fed a standard diet under a 12-hour light/dark cycle (lights on at 6:00 or 7:00). Only healthy, immunocompetent mice that had not participated in previous procedures were used. All fetal surgeries were performed on pregnant Katahdin sheep, obtained from Purdue University (West Lafayette, IN), at gestational ages 77-125 days.
Wild animals	The study did not include wild animals.
Reporting on sex	For mouse models, both adult male and female mice were included. For ovine models, only female pregnant sheep were included for fetal surgeries.
Field-collected samples	The study did not include field-collected samples.
Ethics oversight	Animals were managed according to protocols approved by Northwestern University and University of Chicago Animal Care and Use Committees.

Note that full information on the approval of the study protocol must also be provided in the manuscript.

Plants

Seed stocks	N/A
Novel plant genotypes	N/A
Authentication	N/A